Important Notice

UNIVERSITY OF CALGARY

Time-lapse Seismology to Determine Foamy Oil and Wormhole Footprints in a Heavy Oil Cold Production Reservoir

by

Qiaozhi (Sandy) Chen

A THESIS

SUBMITTED TO THE FACULTY OF GRADUATE STUDIES

IN PARTIAL FULFILLMENT OF THE REQUIREMENTS FOR THE

DEGREE OF MASTER OF SCIENCE

DEPARTMENT OF GEOLOGY AND GEOPHYSICS

CALGARY, ALBERTA

December, 2004

THE UNIVERSITY OF CALGARY
FACULTY OF GRADUATE STUDIES

The undersigned certify that they have read, and recommended to the Faculty of Graduate Studies for acceptance the thesis entitled "Time-lapse Seismology to Determine Foamy Oil and Wormhole Footprints in A Heavy Oil Cold Production Reservoir" submitted by Sandy Chen in partial fulfillment of the requirements for the degree of Master of Science.

Supervisor, Dr. Larry R. Lines
Department of Geology and Geophysics

Dr. Robert R. Stewart
Department of Geology and Geophysics

Dr. Brij Maini
Department of Chemical and Petroleum Engineering

Date

ABSTRACT

Simultaneous extraction of oil and sand during cold production of heavy oil generates high-porosity channels termed “wormholes”. The development of wormholes causes reservoir pressure to fall below the bubble point, resulting in dissolved-gas coming out of solution to form foamy oil. Amplitude anomalies in the vicinity of the borehole observed in time-lapse seismic surveys are possibly a result of the presence of foamy oil and wormholes. These results can be used to image the drainage pattern, which reflects the foamy oil and wormhole footprints, for infill drilling designs. The use of time-lapse reflection seismology for detecting the presence of foamy oil and wormholes is discussed here. This thesis presents one of the first comprehensive seismic modeling studies of these cold production phenomena.

The presence of small amounts of gas within the foamy oil can dramatically decrease the fluid bulk modulus, reducing the *P*-wave velocity of saturated sands. Elastic moduli and velocities, under gas influence, have been modeled to an in-situ reservoir in a Western Canadian heavy oil field. 2D numerical seismic responses of foamy oil zones show amplitude anomalies and traveltime delays when pre- and post-production results are compared.

On the other hand, wormholes, with porosities greater than the critical porosity, can strongly change the rigidity and frame bulk modulus of the reservoir sands, thus resulting in the decrease of both *P*-wave and *S*-wave velocities of the saturated sands. The macroscopic effects of wormholes on *P*-wave and *S*-wave velocities of the

reservoir rock can be observed, when large amounts of sands are produced. 2D numerical models designed to examine cumulative effects of wormholes using both *PP* and *PS* seismic data indicate that *PS* data are better at imaging the wormhole footprints due to its significant impact on *S*-wave velocity. Also, the increase in amplitude anomalies is proportional to wormhole density.

The combined effects of both foamy oil and wormholes are also examined to show the amplitude anomalies and traveltime delays within the drainage regions. Considering that most of the cold production reservoirs are thin, seismic resolution of anomalous areas is highly dependent on frequency bandwidths.

In this thesis, the V_p/V_s values from four different reservoir states have been studied. When compared to the initial reservoir state, V_p/V_s of the post-production reservoir with both foamy oil and wormhole effects can be higher or lower. If the wormhole effect is dominant, V_p/V_s will increase. If the foamy oil effect is dominant, V_p/V_s will decrease. This makes it complicated to analyze the AVO effects under the influence of the foamy oil and wormholes in heavy oil cold production.

ACKNOWLEDGEMENTS

The author would like to express her sincere appreciation to her thesis supervisor Dr. Larry R. Lines not only for his guidance and contribution during this research work, but also for his strong support and encouragement during the years she pursued her MSc degree at the Department of Geology and Geophysics.

Special thanks are offered to Dr. Ron P. Sawatzky and Dr. P.F. Daley for their scholarly assistance. She also would like to thank Ying Zou for her intelligent suggestions and kind help as well as her friendship.

The author thanks the COURSE and CHORUS Projects and the CREWES for their technical and financial support. She also gives thanks to Alberta Research Council for providing valuable data and technical advice.

To the loves of my life: Jin Xie and Lisa Xie

TABLE OF CONTENTS

LIST OF FIGURES

LIST OF TABLES

CHAPTER 1: Introduction to heavy oil cold production

Much of the heavy oil recovery in Western Canada involves steam injection, called 'hot production'. In this process, steam is injected into the reservoir, increasing the temperature of the reservoir and reducing the viscosity of the heavy oil, thus making flow easier and boosting the oil recovery. An alternative to heavy oil production in the field is known as 'cold production', which is a primary non-thermal process in which reservoir temperature is not affected. During the cold production process, sand and oil are produced simultaneously to enhance oil recovery. The cold production process has been economically successful in several unconsolidated heavy oil fields in Alberta and Saskatchewan, Canada (shown in Figure 1.1). This has been due mainly to the development and widespread use of progressive cavity pumps (shown in Figure 1.2). These pumps can generate high pressure to lift the unconsolidated sands to the surface. The progressive cavity pump is designed to facilitate and improve the handling of a viscous and abrasive multiphase fluid, including heavy oil, gas and a large influx of sand (Dunn, et al. 1995). Nevertheless, unlike hot production, cold production has minimal energy requirements and has modest recovery rates. Cold production accounts for the production of 200,000 barrels per day in Western Canada. This process has also been applied in Venezuela and in China.

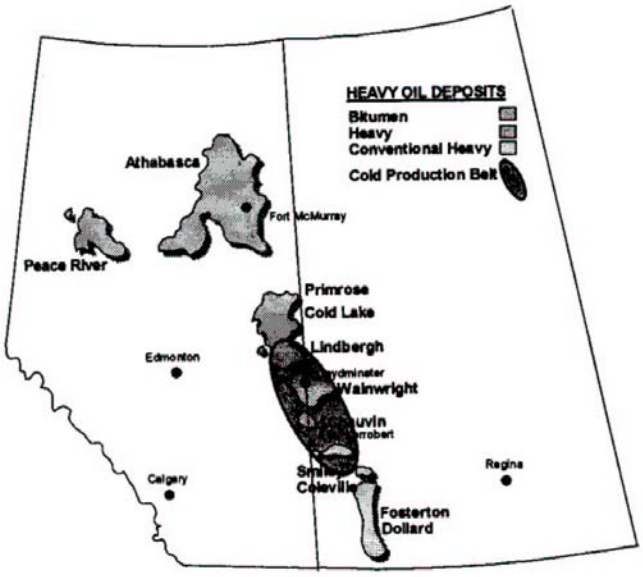

Figure 1.1 Heavy oil deposits in Alberta and Saskatchewan, with an indication of the cold production belt surrounding Lloydminster (Sawatzky et al., 2002). Where the API of cold production heavy oil ranges from 5 to 14.

1.1 Field observations

1.1.1 Reservoir conditions and production rates

Most of the cold production reservoirs are thin with thicknesses ranging from 3m to 7m. It is not efficient to exploit these reservoirs using steam injection. The conditions for the reservoirs where cold production have been applied in Western Canada are given in Table 1.1 (Tremblay, et al. 1999a). In particular, the oil should have enough dissolved gas with a GOR (Gas Oil Ratio) greater than 5%, and sands poorly consolidated with porosities higher than 30% and composed mostly of quartz. The average diameter of the

sands produced by cold production is between 0.1*mm* and 0.25*mm*. Most producing formations in Western Canada belong to the Lower Cretaceous Mannville Groups, having common depths from 400*m* to 800*m*. The reservoir temperature is of the order of 20 degrees centigrade, and the initial reservoir pressure is on the order of 3000 – 5000*kPa,* at the bubble point.

Figure 1.2 A schematic diagram of a cold production oil pump (courtesy of Kudu Oil Well Pumps)

Table 1.1 Reservoir conditions of cold production fields in Alberta and Saskatchewan

	PanCanadian	Mobil	Suncor	Ranger	Texaco
Formation	Mannville	Mannville	Clearwater	clearwater	Mannville
Field	Lindberg, Frog Lake	Celtic	Burnt Lake	Elk Point	Frog Lake
Oil saturation			80	87	70 - 80
Gas/oil ratio m^3/m^3		10	5 - 11.0	11 - 15.2	10
Viscosity Pre (live) @cp	3,000-10,000	1,200-3,000	40,000 (dead)	2,000-55,000	20,000-50,000
Pressure MPa	4	3.3	3.3	3.8	2.8 - 3.4
Permeability darcies	1.5 - 2.5	0.5 - 4.0	2		1.0 - 5.0
API gravity	12 - 14		12	11	
Net pay	14	3 - 5	20	11 - 14	4 - 11
Porosity	32	33	34	34	33

(Tremblay et al., 1999)

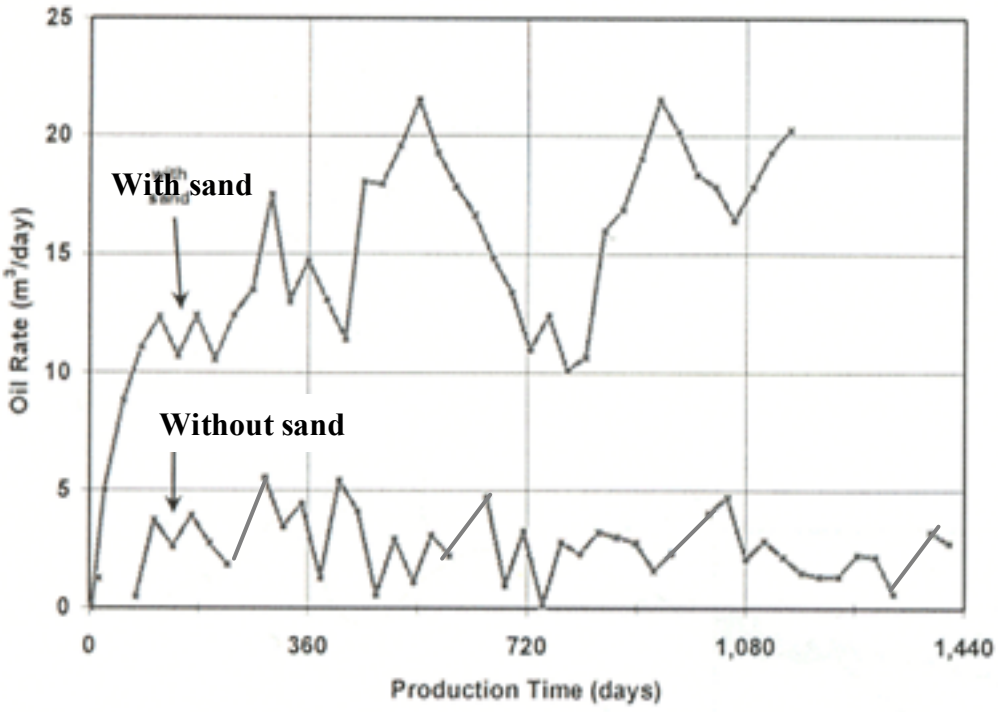

Figure 1.3 Comparison of oil production rates for two wells in the same Edam pool – one with sand production and one without (Sawatzky et al., 2002)

With sand production, the cold production process improves oil production rates substantially compared to the primary production rates when sand is not produced. Figure 1.3 compares the production rates of sand production and non-sand production for two wells in the Edam field, Alberta (Sawatzky, et al. 2002). Producing sand improves oil production rate by an order of magnitude compared with the average production rate of non-sand production.

Most of the sand is extracted during the first six or twelve months of production, where the sand cuts can be high, varying form 10% to 40% of the total volume of the fluids and sand slurry. After that, the sand cuts tends to be low and stable, less than 5%, at which time oil production dominates (Tremblay et al., 1999a). The sand cuts are normally measured in the field by centrifuging a sample of the produced oil, water and sand slurry. The ratio of the settled sand volume to the total volume of the sample would then be quoted as the sand cut. In the Lindbergh and Frog Lake field, 40 wells have been used in statistics that indicate that an average of 9000 m^3 of cumulative gross fluid production can result in an average of 200 $m^3$of sand production within 1000 days (Metwally, et al. 1995). In general, the initial rate of sand production increases with increasing oil viscosity and permeability. The cumulative sand production is proportional to the cumulative oil production.

1.1.2 Post-production logs and Injection test

In Metwally's paper, a well in Lindbergh, which had produced over 39000 cubic meters of fluid and over 500 cubic meters of sand from a perforated interval of 15*m* has been employed to test the near wellbore reservoir condition changes. Compensated neutron and gamma ray logs were run to compare post-production log response to open hole response. In Figure 1.4, the post-production compensated neutron log showed four zones with porosity of 10-25% higher than the original open hole logs. The peak porosity in the post-production log was about 48%.

After the logging, a slug of radioactive tracer was injected after water injection was terminated. Tracer logs were run following the pressure fall-off to determine which zones were accepting the injected fluid. It indicated that the majority of the injected tracer entered a single discrete zone in the upper perforations. Figure 1.5 showed these zones on post-tracer gamma ray logs. A tracer test run by Amoco (Squires, 1993) also showed that the transit time between wells 400*m* apart was as small as 1 hour. A fluorescent dye was injected at a rate of 30 cubic meters per day. The dye concentration had not changed indicating that it flowed through an open channel and not through a porous medium where it would be adsorbed. This may explain several reports of losing circulation during drilling close to wells which produced a lot of sand.

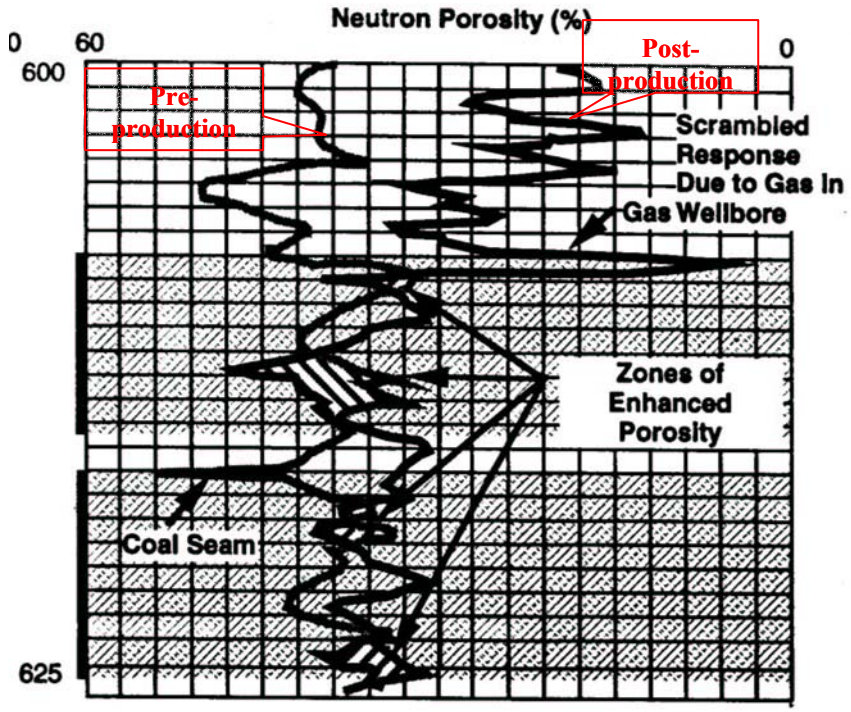

Figure 1.4 Pre- and post-Neutron porosity logs, showing four enhanced porosity zones

(modified after Metwally et al., 1995)

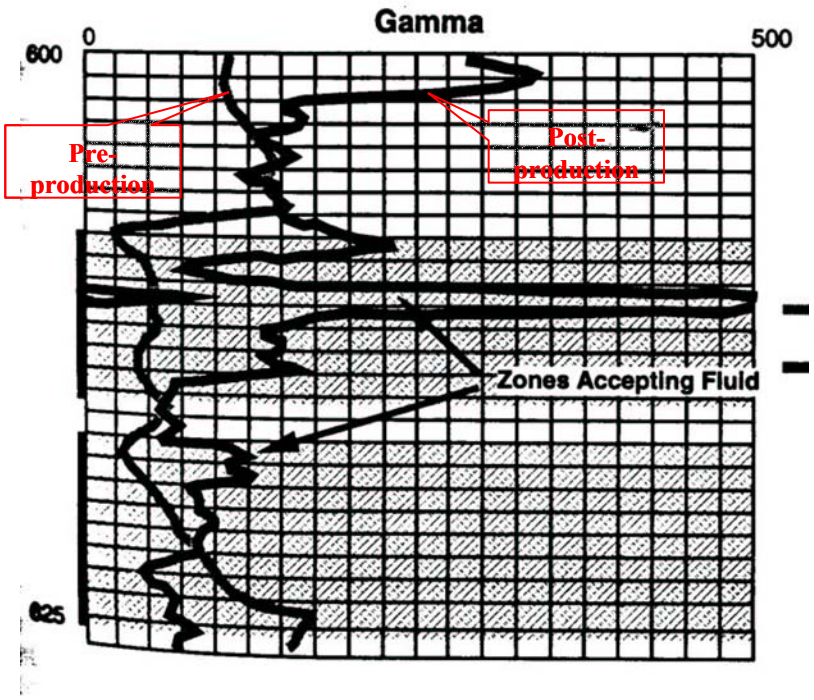

Figure 1.5 Pre- and post-Gamma ray logs, showing zones accepting fluid after tracer test (modified after Metwally et al., 1995)

Based on the tracer test and field observations, we believe that there could have developed some high permeability and porosity channel, called ‘wormholes’, within the reservoir. The wormholes can be considered as small diameter, high porosity pipes, extending far from wellbores and creating interconnection between the well and the reservoir. In this thesis, we’ll focus on seismic modeling of the hypothetic wormholes.

1.2 Mechanism of cold production

1.2.1 Foamy oil drive

Significant increases in oil recovery with increasing rates of pressure depletion were observed in most fields. When the reservoir pressure drops below bubble point, exsolved gas in live heavy oil comes out of solution as bubbles. The gas evolves slowly, but continuous phase coalescence is impeded by capillary effects and high viscosity, keeping the bubbles separate. Thus, the trapped gas bubbles within the heavy oil form the foamy oil, which is a foamy or emulsive state (shown in Figure 1.6). Unlike normal two-phase flow that requires a fluid phase to become continuous before it becomes mobile, foamy oil flow involves the flow of dispersed gas bubbles. It is believed that such dispersed flow of gas is responsible for unexpectedly high recovery factors often seen in cold production projects (Maini, 2004). Figure 1.7 shows that the formation of foamy oil with separated gas bubbles, increases the fluid volume within the reservoir, forcing grains apart, such that remain a relatively high pressure exists to drive both oil and gas to the wells through wormholes. It appears that the foamy oil contributes significantly to the pressure support in the reservoir. Therefore, foamy oil generation resulting from the initial reservoir pressure reduction provides the necessary support mechanism to sustain the observed high oil recovery (Metwally, et al. 1995).

Figure 1.6 Foamy oil (D. Greenidge, ESSO, private communication)

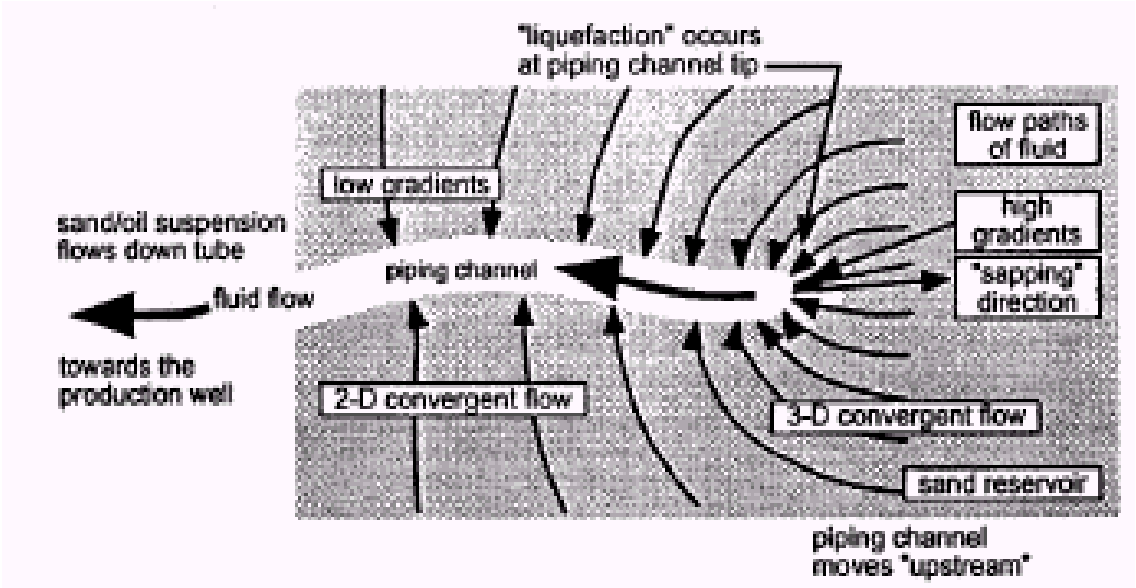

Figure 1.7 Foamy oil drive mechanism (Dusseault, 1994)

1.2.2 Wormhole network growth

Sand production leads to the creation of a high-porosity, disturbed zone supplying a slurry of sand and fluid to the wellbore. Also tracer tests in the field have indicated that there are some open channels with unknown geometry, termed ‘ wormholes’, developing in the reservoir. Several physical lab simulations and numerical simulations have been conducted to induce the development of wormholes. Tremblay, et al (1999b) monitored a wormhole using solution-gas drive in a sand pack with a length of 85*cm*, a width of 10 *cm*, and 32% porosity. Figure 1.8 shows the wormhole growth with pressure depletion, corresponding to the initial state and, 20 and 47 days after the start of pressure reduction, respectively, from above to bottom. Here, the porosity of wormholes could be greater than 40%, and the zone of highest porosity is close to the wellbores. Tremblay also hypothesized that wormhole diameters could range from the order of 10*cm* to one meter as the maximum size in the field.

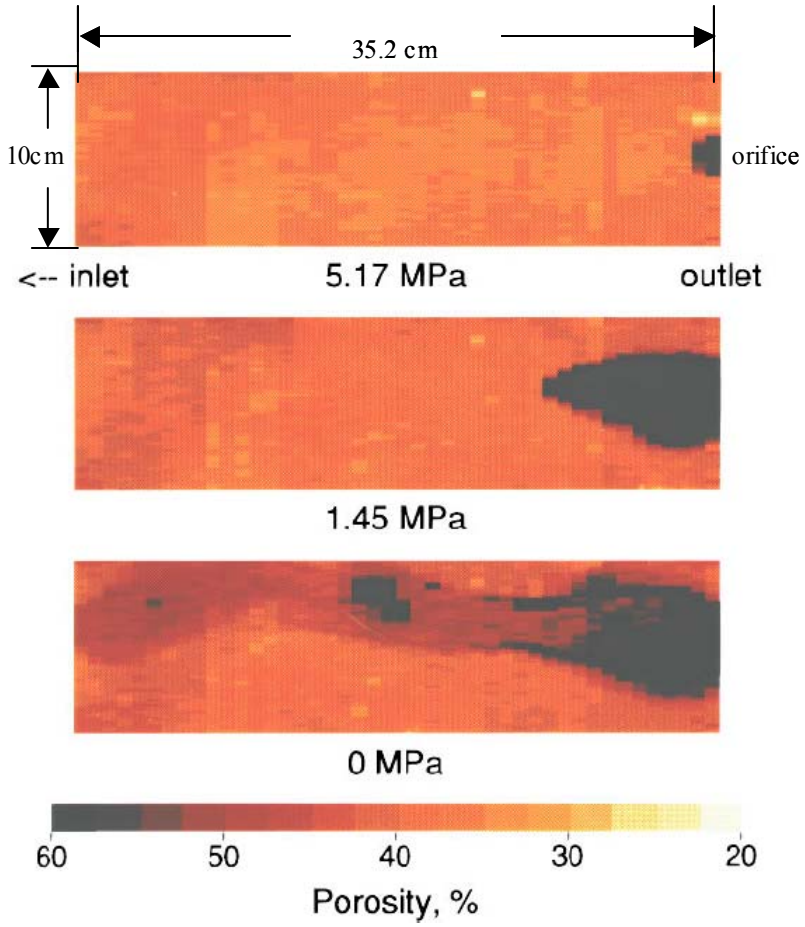

Figure 1.8 CT scanned longitudinal sections of the sandpack with wormhole growth. Top image: before pressure depletion; middle image: 20 days after start of pressure depletion; bottom image: 47 days after start of pressure depletion (Tremblay, et al. 1999b)

Both tracer test and lab simulations show that wormholes likely grow within a certain layer within net pay zones. Sawatzky et al. (2002) believe that wormholes grow in unconsolidated, clean sand layers within the net pay zone, along the highest pressure gradient between the borehole and the tip of the wormhole. The radius of wormhole

zones can be greater than 100*m* based on the numerical simulation results in Yuan et al. (1999), by matching the production history of the field. Also the results fit some field observations. Yuan et al also predicted that wormhole diameter is a function of distance from the wellbore, decreasing in diameter away from the boreholes.

In reality, wormholes could grow anywhere within the pay zone. Yuan extended the probabilistic active walker model, which describes the concept of the random walk model, to simplify the wormhole zone as a thin 'pancake' layer, where wormholes grow randomly in a radial pattern. Miller (2001) also illustrated a similar wormhole network pattern, like the root system in Figure 1.9. Therefore, a wormhole network could create an interconnection between wellbores and reservoirs, providing low resistance drainage paths like fractures, and supplying most of the produced fluids. Only a small fraction of the total production comes from outside this region (Metwally, 1995).

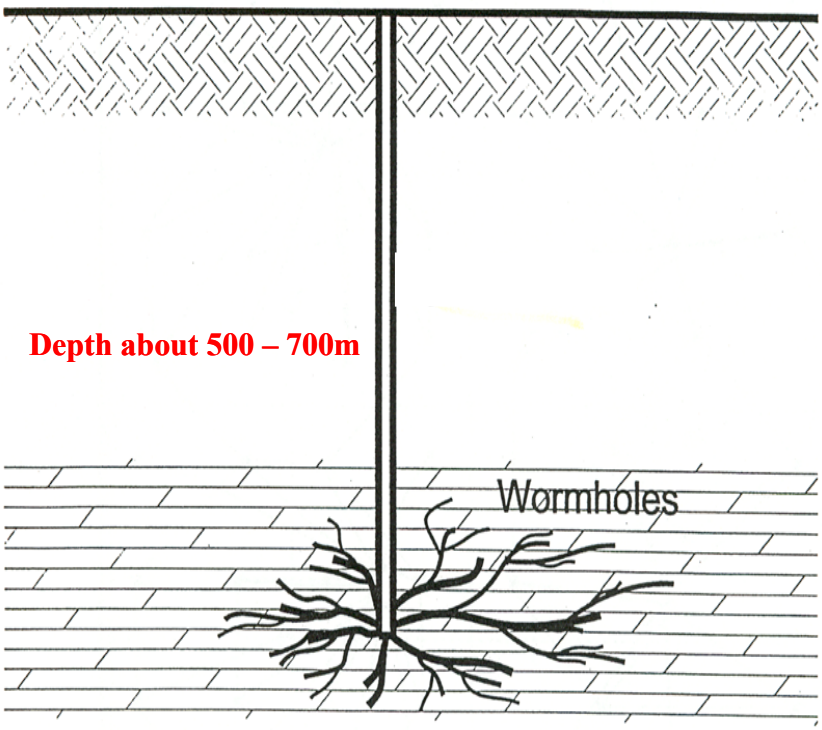

Figure 1.9 Wormhole growing pattern in the reservoir (modified after Miller, et al. 2001)

1.3 Time-lapse seismology and cold production

Time-lapse seismology plays a major role in monitoring heavy oil 'hot' production by delineating the steam front, and has now becomes a standard reservoir characterization tool. Engineers expect that 3D time-lapse seismology could be a tool implemented in the imaging of the drainage pattern, caused by foamy oil and the presence of wormholes, and provide useful information to design infill drilling and development plans in the fields. Sawatzky et al. (2002) showed a most likely drainage footprint scenario for some cold production wells in a small southwestern Saskatchewan

heavy oil pool (shown in Figure 1.10), where drainage regions appear to be elongated around the borehole. Two infill locations have been recommended to be located outside of the drainage zones with the help of the monitored drainage map.

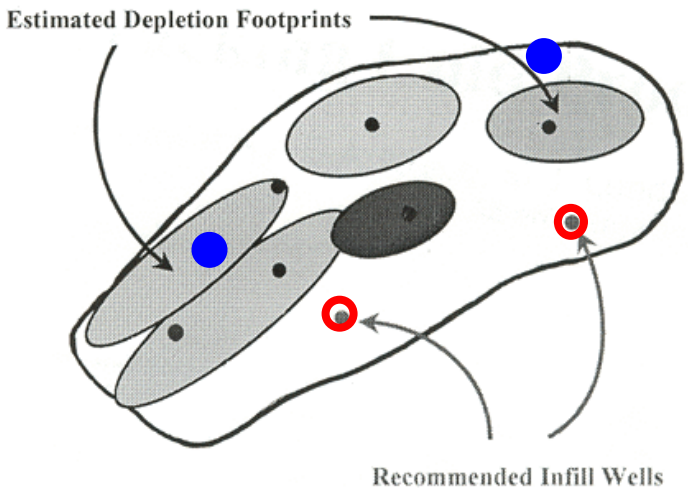

Figure 1.10 Drainage footprint scenario for the cold production wells in a small southwest Saskatchewan heavy oil pool (modified after Sawatzky et al., 2002). The blue dots represent proposed infills, the red circles are recommended infill locations using the drainage footprints in gray coloring.

Mayo (1996) showed a 3D time-lapse seismic survey with some amplitude anomalies around the boreholes in Provost Upper Mannville BB Pool in the Lloydminster cold production field (shown in Figure 1.11). The 3D survey was acquired 9-years after the start of the production. These amplitude anomalies enlighten the possible application

of time-lapse seismic techniques for imaging the drainage footprints of cold production reservoir, due to the presence of foamy oil and wormholes.

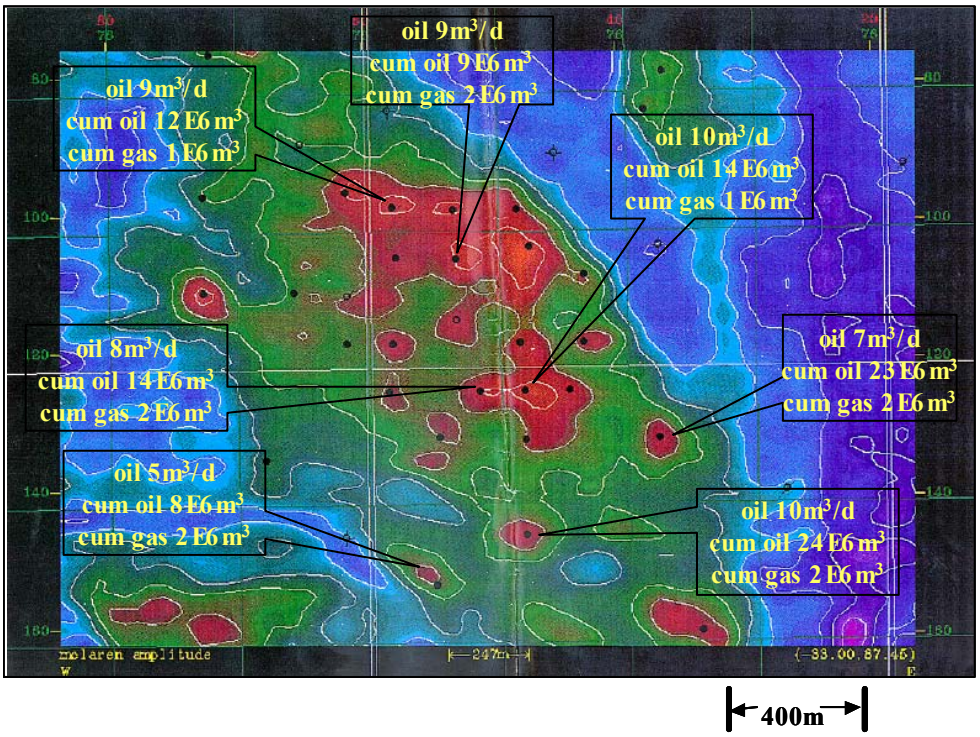

Figure 1.11 3D horizon amplitude map in Provost Upper Mannville BB Pool, Lloydminster after 9-year of production. Red coloring represents strongly negative amplitude anomalies due to sand production. (modified after Mayo, 1996)

Based on the laboratory experiments, Domenico et al. (1976) demonstrated that the compressional velocity (V_p) drops significantly with the presence of a small amount of gas in the pore fluid, which commonly caused “bright spots” on seismic responses. On the other hand, the presence of wormholes could affect the stress and rigidity of sand matrix in the reservoir, leading to rock property changes, such as bulk and shear modulus changes. These changes also could result in the velocity variations of the reservoir rocks. Therefore, both wormholes and foamy oil are probably two key factors causing the amplitude anomalies observed on seismic data, which could represent the footprints of the drainage pattern and wormhole channel distribution within the reservoir. The purpose of this thesis study is to address why and how foamy oil and wormholes can be detected using time-lapse seismology, and find out which of these two factors plays a dominant role.

CHAPTER 2: Simplified Geological Model of Heavy Oil Cold Production

2.1 Typical drainage model with wormholes and foamy oil

Based on the understanding of wormhole growth pattern in Chapter 1, it is known that wormholes likely develop at a certain layer within net pay zones. They could extend vertically through part or the entire net pay zones, which depends on the thickness of the net pays. Laterally, the length of wormholes can extend as far as 100m or more from the well. Also wormholes grow in a 3D radial pattern like a tree root system within a specific layer. They appear to have diameters on the order of centimeters to the maximum of 1 meter based on the lab simulations (Tremblay, personal conversation).

With the growth of wormholes, there is also a significant change in the reservoir pressure within drainage regions. The drainage region can be defined as the region where the reservoir pressure is reduced. Equivalently, you can think of it as the region from which the oil is produced. Without wormholes, there would still be a drainage region. However, when wormholes are generated, the drainage region could be larger than the normally producing drainage zone without wormholes. The length of wormholes could be employed to define the lateral extent of the drainage region. Wormholes have a very high permeability, so the pore pressure is low within the wormhole. Therefore, the pressure

gradient at the tip of a wormhole is relatively high, resulting in the growth of wormholes. Thus, it causes a region of the reservoir in front of the wormholes to be depressurized. And this region does not extend very far from the tip of the wormholes based on the laboratory observations of Sawatzky at ARC (Alberta Research Council). Wormholes can continue to grow as long as the pressure gradient in the fluid is large enough to cause the sand matrix to fail. There is a critical pressure gradient, below which the sand will not fail, and wormholes stop growing. Therefore, the length of wormholes can be used to define the lateral extent of the drainage regions in a simplified model.

As we mentioned above that the wormholes develop within a certain layer of net pay zone, and the definition of the vertical extent of a wormhole layer can be perceptive. The thickness of this layer versus the pay thickness can vary from 0.1 to 1.0 according to Sawatzky. However, the layers above or below the wormhole layer within the net pay zone can be depressurized because most net pay zones of cold production reservoirs are thin, less than 10m thick.

Therefore, a simplified drainage model of heavy oil cold production with the presence of wormholes and foamy oil can be built. It is assumed that the drainage zone is a cylinder around boreholes. A schematic of this is shown in Figure 2.1, a 3D map view

on the top, and a 2D cross-section at the bottom. The volume of the drainage zone is determined by the length of wormholes and the net pay thickness. The wormhole density is highest close to the borehole. Beyond the drainage region, is the region that remains in the initial reservoir state without wormholes and foamy oil. In reality, there is a transition zone between the drainage region and the undisturbed region. It is probably fairly narrow, in the range of 10 – 20 meters (Sawatzky, personal conversation). With the presence of wormholes, this transition zone is even sharper. In our geological model, this transition zone has been ignored to simplify modeling.

Before production, most of the heavy oil cold-production reservoirs are highly saturated with oil, varying between 70% and 90%, the remainder being water. After the start of the production, with sand extraction and wormhole growth, the reservoir pressure drops below the bubble point. This results in gas coming out of solution as bubbles, forming foamy oil. Thus, the initial fluid phase changes to oil, water, and foamy oil with gas bubbles. Therefore, the fluid phases within the drainage region are highly disturbed with the presence of foamy oil, and can be significantly different from the initial reservoir state of oil and water. In addition, the development of wormholes can change the physical properties of the reservoir sands as a consequence of the sand extraction.

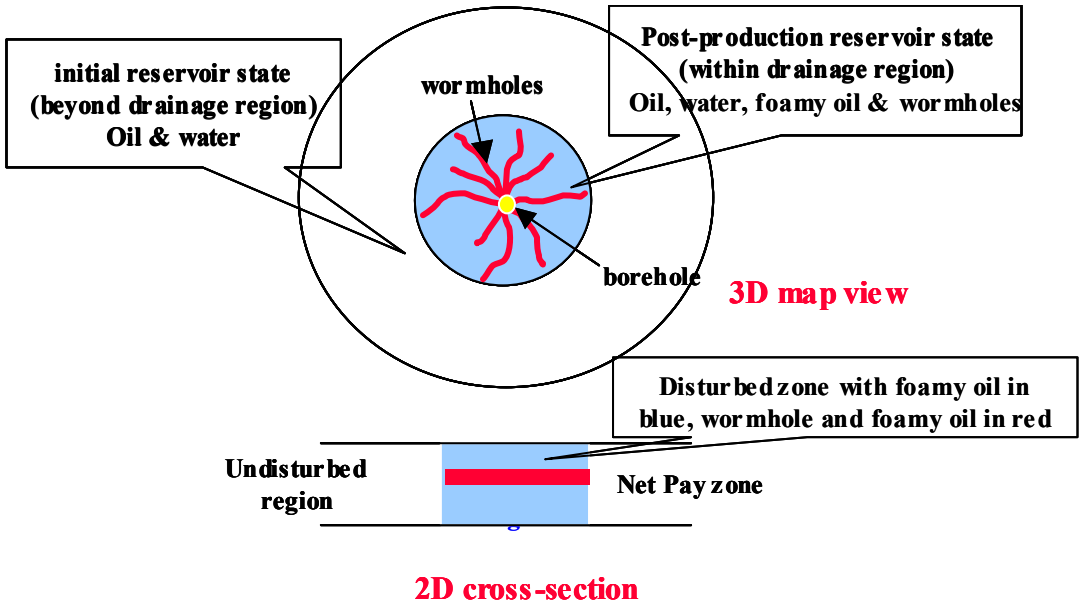

Figure 2.1 Simplified drainage model of cold production reservoir, with a 3D map view above, and 2D cross-section below. In the 2D cross-section, the disturbed drainage zone consists of the zone in blue with foamy oil effects only, and the zone in red with both foamy oil and wormhole effects, which could occupy the entire net pay zone when the pay thickness is small.

2.2 Seismic resolutions and wormholes

Lines, et al. (2003) discussed the relation of seismic resolution and wormholes. In this paper, an ideal 2D wormhole numerical model (Figure 2.2) was built to exam the seismic frequency effects on imaging individual wormholes. Figure 2.2 shows that wormholes randomly grow in a radial pattern from the well in a 2D profile, with a diameter of 10 centimeters. Finite-difference modelling was employed to generate

synthetic seismograms of this numerical model, using wavelets with a dominant frequency of 3000*Hz* and 185*Hz*, respectively. Figure 2.3 shows a clear image of individual wormholes using ultrahigh frequencies. When bandpassing this seismic data using a filter with a 185*Hz* peak frequency, only a blurred image of wormholes can be seen (Figure 2.4).

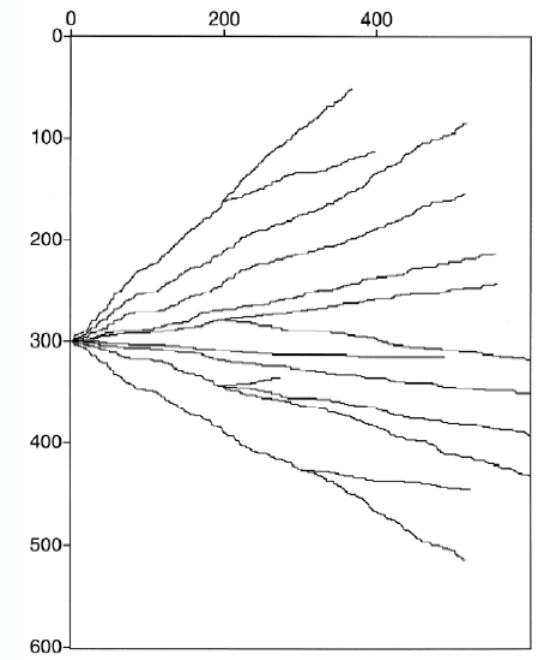

Figure 2.2 An ideal 2D wormhole model of dimensions 60 × 60*m* (from Lines,et al. 2003)

Individual wormholes can be detected with these extremely high frequencies as shown in Figure 2.3. However, it would be very unusual to see such high frequencies in field data, except possibly in cross-borehole seismology. Therefore, we could conclude

that using surface seismic techniques can only image the cumulative response of wormholes, when a large amount of wormholes present.

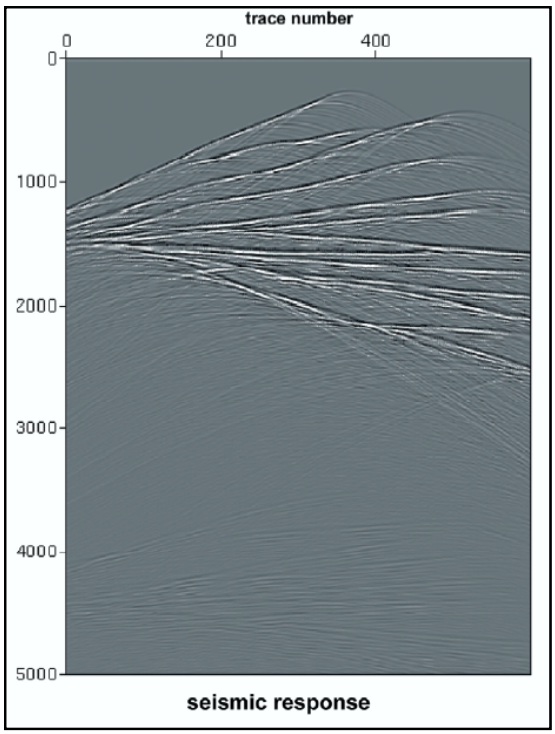

Figure 2.3 Synthetic seismogram of the model in Figure 2.2 with ultrahigh dominant frequency of 3000*Hz*. The sample interval on vertical axis is 0.01*ms* and trace spacing is 10*cm*. (Lines, et al. 2003)

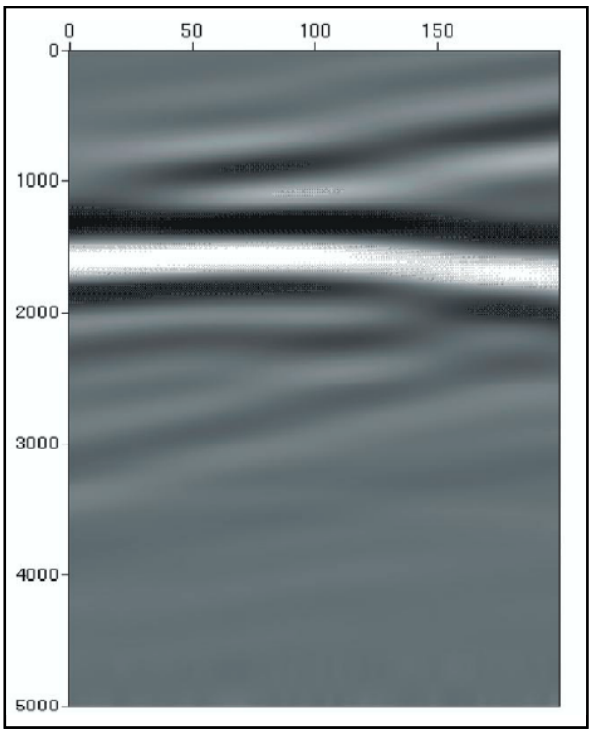

Figure 2.4 Synthetic seismogram for the left 20*m* of the seismogram in Figure 2.3 high-cut filtered to 185*Hz*. (Lines, et al. 2003)

Actually, imaging wormholes is involved in the matter of 3D seismic techniques, because wormholes grow like tubes in a 3D radial pattern. Therefore, an ultrahigh frequency is also required to collapse the Fresnel zone due to the small diameters of wormholes. However, we can still image the cumulative response of wormholes when they have a high density.

2.3 Chapter summary

Seismic amplitude anomalies around the borehole have been observed in the Lloydminster heavy oil cold production field, shown in Figure 1.11. Mayo (1996) tends to believe that any seismic anomalies could be attributed solely to the presence of foamy oil, which fills in the drainage region. However, based on the studies of Lines, et al (2003), wormholes can be considered as another key factor contributing to the amplitude anomalies, when large amount of sands are produced, and a high density of wormholes exists in the drainage region. The reasons, why both foamy oil and wormholes can cause anomalous seismic responses, will be discussed in subsequent chapters.

CHAPTER 3: Fundamentals of Seismic Rock Physics

During the past 50 years or so, tremendous progress has been made in studying physical properties of rocks and minerals in relation to seismic exploration. In exploration seismology, seismic waves bring out subsurface rock and fluid information in the form of traveltime, reflection amplitudes, and phase variations. Seismic data are now commonly analyzed for determining lithology, porosity, pore fluids, and saturations, because rock physics bridges seismic data and reservoir properties and parameters. Seismic properties are affected in complex ways by many reservoir properties, such as pressure, temperature, saturation, fluid type, porosity, pore type, etc (Wang, 2001). These factors are often interrelated or coupled with each other. In order to understand the rock physics application to seismic interpretation, the investigation of the effect of single factor can be studied while holding all other factors. Wang, et al. (2001) has discussed the effects of some of the main rock physical parameters on seismic properties.

3.1 Fluid substitution: the Gassmann Equation

The Gassmann (1951) equation has been used for calculating the effect of fluid substitution on seismic properties using the matrix properties. It predicts the bulk

modulus of a fluid-saturated porous medium using the known bulk moduli of the solid matrix, the frame and the pore fluid, in the following manner:

$$K_u = K_d + \frac{(1 - K_d/K_s)^2}{\frac{\phi}{K_f} + \frac{1-\phi}{K_s} - \frac{K_d}{K_s^2}}, \tag{3.1}$$

where, K_μ, K_d, K_s, K_f, and ϕ are the saturated porous rock bulk modulus, the frame rock bulk modulus, the matrix bulk modulus, the fluid bulk modulus and the porosity. The shear modulus μ of the saturated rock is not affected by fluid saturation, so that

$$\mu = \mu_d \ , \tag{3.2}$$

where μ_d is the frame shear modulus. It is important to point out that the frame moduli are not the same as the dry moduli (Wang, et al. 2001). In the correct use of the Gassmann equation, frame moduli should be measured at irreducible saturation conditions of the wetting fluid (normally water). The overdrying of a rock in the laboratory will result in erroneous results for the purposes of Gassmann's equation..

P-wave and *S*-wave velocities, V_p and V_s, for an isotropic, homogeneous, elastic material are given by

$$V_p = \sqrt{\frac{K_u + 4\mu/3}{\rho_u}}, \tag{3.3}$$

$$V_s = \sqrt{\frac{\mu}{\rho_u}} . \tag{3.4}$$

The saturated rock bulk density can be calculated as:

$$\rho_u = \rho_s(1-\phi) + \rho_f\phi . \tag{3.5}$$

where ρ_s, ρ_u and ρ_f are the densities of solid grains, saturated reservoir rock and the fluid mixture at reservoir conditions.

Equations 3.1 to 3.5 establish the relationships between the rock moduli and the seismic velocities. The accuracy of the Gassmann equation for calculating the seismic velocities is based on some basic assumptions (Wang, 2001):

1) The rock (both the matrix and the frame) is macroscopically homogeneous.
2) All the pores are interconnected or communicating.
3) The pores are filled with a frictionless fluid (liquid, gas, or mixture).
4) The pore fluid does not interact with the solid in a way that would soften or harden the frame.

Assumption (1) is common to many theories of wave propagation in porous media. The frequency ranges from seismic to laboratory generally assure that the wavelengths are long enough compared to the grain and pore size. Assumption (2) implies that the porosity and permeability are high and there are no isolated or poorly

connected pores in the rock. For seismic waves, however, only unconsolidated sands can approximately meet this assumption because of the sand's high porosity and permeability (Wang, 2001). Assumption (3) implies that the viscosity of the saturating fluid is zero. In reality, all fluids have finite viscosities, so, most calculations using the Gassmann equation will violate this assumption. This may be the most questionable assumption for heavy oil. Assumption (4) eliminates any effects of chemical/physical interactions between the rock matrix and the pore fluid. It is difficult to give an explicit description for the interaction.

Wang compared the Gassmann results and laboratory results of the effect of the fluid displacement in several ways. He concluded that the Gassmann-predicted and the laboratory measured effects of fluid displacement on seismic properties might be directly applied to 4D seismic feasibility studies and interpretations.

3.2 Effects of pressure

Generally, the *P*-wave and *S*-wave seismic velocities increase with an increase in the reservoir pressure. Here, the reservoir pressure is referred to the effective pressure P_e, given by (Wang, 2001)

$$P_e = P_c - nP_p \qquad (n \leq 1) \qquad (3.6)$$

where P_c is the confining pressure or overburden pressure, and P_p is the pore pressure. As shown in Figure 3.1 (Castagna and Backus, 1993, and Wang, 2001) the *P*-wave and *S*-wave velocities are functions of the effective pressure. The typical behaviours of most porous rocks are for velocities to increase rapidly at low pressures and more slowly at high pressures.

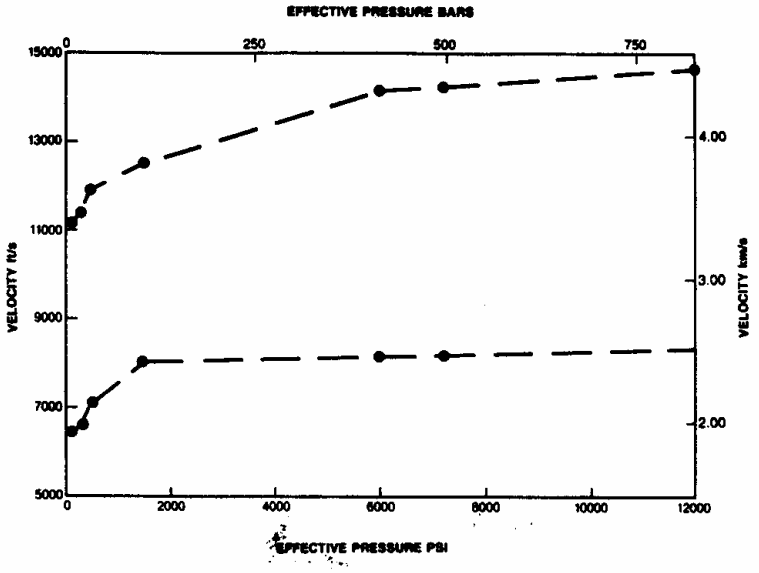

Figure 3.1 Variation of *P*- and *S*- wave velocity with pressure for water-saturated sandstones with a porosity of 19% from a depth of 3607*m* (Castagna et al., 1993)

During the development of the reservoir, hydrocarbons have been produced, or water is injected into the reservoir. These can significantly change the pore pressure of the reservoir, resulting in the variation of the effective pressure. Thus, seismic *P*-wave

and *S*-wave velocities are affected. This is important for time-lapse seismic analysis to detect the reservoir property changes. Batzle and Wang (1992) established some empirical equations to describe the relations of the effective pressure and fluid displacement, which will be discussed later.

3.3 Effects of temperature

Seismic velocities and impedances decrease only slightly in rocks saturated with gas or water as the temperature increases with the ranges commonly encountered in the exploration. When a rock is saturated with oil, however, seismic velocities may decrease by large amounts with increasing temperature, especially in unconsolidated sands with heavy oil (Wang, 2001). Because heavy oil are viscous, there exists a strong interfacial force between the oil and the rock grains. As temperature increases, oil viscosity and thee interfacial force decrease, loosing up the sand grains so that both the bulk modulus and shear rigidity decrease. That is the reason why time-lapse seismology has been popularly used in the heavy oil steam-injection reservoir to image the steam front during production, because the high temperature caused by injected vapors can significantly reduce the seismic velocities of the reservoir sands. However, the heavy oil cold production does not involve reservoir temperature changes during production. Therefore,

temperature cannot be applied to detecting reservoir properties in the cold production case.

3.4 Effects of porosity

Determining accurate relations between porosity and seismic wave velocities in porous rocks has been an important topic of rock physics for decades, because seismic data can be used to infer porosity and porosity-related properties (e.g. permeability, saturation) in situ. Approaches to establishing porosity-velocity or porosity-modulus relations can be categorized as empirical relations and theoretical bounds (Nur, et al. 1998).

3.4.1Empirical relations of velocity-porosity or modulus-porosity

The well-known velocity-porosity transform is the Wyllie et al. (1956) time-average equation (WGG equation) given by

$$1/V_p = (1-\phi)/V_m + \phi/V_f \quad . \tag{3.7}$$

Castagna et al. believe that the WGG equation is often used in well consolidated sandstones for porosity determination from well logs. They also believe this equation can cause erroneous results for gas sands.

For most rocks, there is a critical porosity ϕ_c, which is defined as a porosity that separates their mechanical and acoustic behaviour into two distinct domains (Mavko and Mukerji, 1998). In other words, the critical porosity can be thought of as a critical value separating the compressibility and rigidity of saturated rocks into two distinct domains: frame-supported and fluid-supported. Different rocks have their particular critical porosities. Figure 3.2 shows the critical porosity of sandstone.

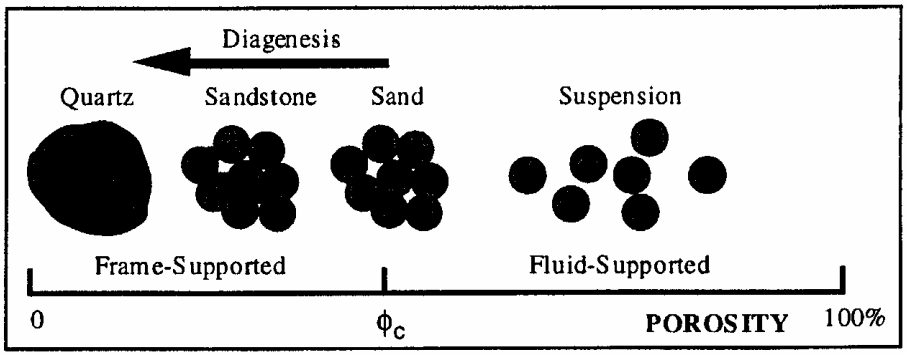

Figure 3.2 Physical meaning of critical porosity (Nur et al., 1998)

For porosities less than ϕ_c, the mineral grains are consolidated, with the frame-supported state. For porosities greater than ϕ_c, the grains are in a suspension, with the fluid-supported state. And Figure 3.3 shows that critical porosity in clean sandstones separates the consolidated-rock domain from the suspension domain. The mechanical behaviour drastically differs between these two domains from the point of view of bulk modulus.

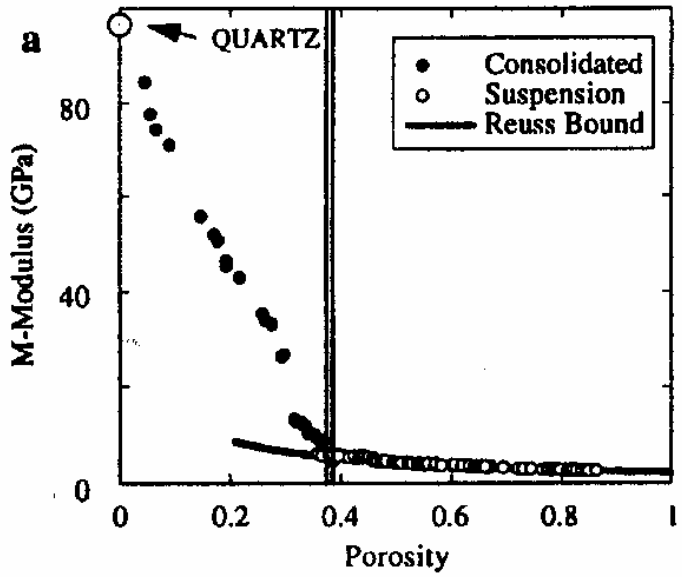

Figure 3.3 A critical porosity (about 38%) in clean sandstones separates the consolidated-rock domain form the suspension domain where the Reuss Bound is defined in equation 3.11; M-Modulus is the compressional-wave modulus, is equal to ρV_p^2 (Nur et al., 1998).

Murphy, et al (1993) conducted careful experiments on pure quartz to demonstrate two simplifying constructive relationships. First, the bulk and shear frame moduli are simple functions of the porosity. Second, the ratio of bulk and shear frame moduli is a constant of 0.9 and independent of the porosity. Murphy et al. also decomposed the Gassmann equation as:

$$K_{\mu} = K_d + K_p, \tag{3.8}$$

where K_d is the frame bulk modulus, a strong function of porosity, and K_p is defined as pore space modulus, given by

$$K_p = \frac{(1 - K_d / K_s)^2}{\frac{\phi}{K_f} + \frac{1-\phi}{K_s} - \frac{K_d}{K_s{}^2}}. \tag{3.9}$$

Let $\alpha = 1 - K_d / K_s$, then

$$K_p = \frac{\alpha^2}{\frac{\phi}{K_f} + \frac{\alpha - \phi}{K_s}}. \tag{3.10}$$

The compliance α of the frame is relative to that of the solid grains. In practice, the contribution of K_p is quite significant to V_p at high porosity, whereas K_d is relatively weak. At low porosities, where $K_d \rightarrow K_s$ and $\alpha \rightarrow 0$, the effect of K_p is insignificant. The Gassmann relation remains valid through the consolidation transition at ϕ_c. If $\phi > \phi_c$ and the grains are suspended in the fluid, then K_d=0, μ=0, α=1, and K_p is given by Wood's (1941) formula (Reuss Lower Bound):

$$\frac{1}{K_p} = \frac{\phi}{K_f} + \frac{1-\phi}{K_s} \ . \tag{3.11}$$

In this case, the fluid and solid grains are compressed as if they are springs being added in series. In other words, the solid grains are suspended within the fluid. Here, K_p is exactly equal to the Reuss lower bound.

For the frame bulk modulus K_d and shear modulus μ, Murphy et al. also compiled high quality laboratory data on gas saturated, pure quartz sands and sandstones (with $SiO_2 \geq 0.98$) at high effective pressures, roughly $50MPa$ and established the relations between the frame bulk and shear moduli with porosity. The best empirical fit has:

$$K_d = 38.18 * (1 - 3.39\phi + 1.95\phi^2); \qquad \phi \le 0.35$$

$$K_d = \exp(-62.60\phi + 22.58); \qquad \phi > 0.35 \tag{3.12}$$

$$\mu = 42.65(1 - 3.48\phi + 2.19\phi^2); \qquad \phi \le 0.35$$

$$\mu = \exp(-62.69\phi + 22.73); \qquad \phi > 0.35 \tag{3.13}$$

These empirical relations demonstrate a remarkably clean dependence of the elastic moduli on porosity, respectively divided into both the frame-supported and fluid-supported domains based on the critical porosity. These equations can be applied to the computation of the frame and shear moduli of the wormholes, which are composed of the suspension sand grains and mixed fluids with a possible porosity greater than the critical porosity.

3.4.2 Bounds relations of modulus-porosity

The known theoretical bounds to describe the modulus-porosity relations are Reuss lower bounds and Voigt upper bounds (Nur et al. 1998). The concept of the fluid mixture theory (uniform and patchy saturation states), which describes the mixture of two fluid phases, can be used to describe the mixture of a saturated rock. A porous rock can be thought of as a two-phase mixture – void space and rock matrix. Therefore, the Upper and Lower bounds may be applied to calculating the ranges of bulk and shear moduli of

any porous rock (Downton, 2001). The bulk modulus and shear modulus of a saturated rock will lie between the Reuss lower bound and the Voigt upper bound as :

$$K_R \le K \le K_V, \quad \mu_R \le \mu \le \mu_V, \tag{3.14}$$

where, K_R, K_V, μ_R, μ_V are respectively bulk and shear moduli of the Reuss and Voigt Bounds. The Reuss lower bound for bulk modulus is given by

$$\frac{1}{K_R} = \frac{1-\phi}{K_s} + \frac{\phi}{K_f}. \tag{3.15}$$

and the Voigt upper bound for bulk modulus is given by

$$K_V = (1-\phi)K_s + \phi K_f. \tag{3.16}$$

The lower bound of shear modulus μ will be zero, because the shear wave can not propagate in fluids. The (*Voigt*) upper bound of shear modulus is given by

$$\mu_V = (1-\phi)\mu_s, \tag{3.17}$$

Where, K_s, K_f, μ_s are the matrix modulus, fluid modulus and shear modulus. However, the bounds do not give specific modulus or velocity values at a given porosity. Empirical relations are required to be employed.

CHAPTER 4: Foamy oil and wormhole effects on seismic properties in a Lloydminster cold production field

Seismic amplitude anomalies observed in the vicinity of the boreholes in time-lapse seismic surveys are possibly a result of the presence of foamy oil and wormholes. In order to better understand the effects of foamy oil and wormholes, we will discuss the foamy oil and wormhole effects respectively on seismic properties in this chapter. In each case, we assume that the other effect is ignored. In other words, there is no sand extracted from the reservoir and the average porosity of the reservoir sands remains consistent when foamy oil effects are discussed. On the other hand, there are no free gas effects on seismic properties when wormhole effects are presented.

4.1 In-situ reservoir parameters of a heavy oil cold production field

Tremblay at al. (1999) showed the general reservoir conditions of heavy oil cold production fields in Alberta and Saskachewan in Table 1.1. Sawatzky et al. (2002) also summarized that most of the cold production reservoirs are thin, with net pay thickness less than 10 *m*, and with a depth ranging from 400 to 800 *m*. They also pointed out that the initial reservoir pressure is on the order of 3000 – 3500 *kPa*, and the pressure falls to levels in the range of 500 – 1500 *kPa* after being drained by a mature cold production

well. The drainage area will contain exsolved gas from the depressurized heavy oil, with saturations on the order of 5 – 20%. Table 4.1 provided by Alberta Research Council, shows the in-situ reservoir parameters from a 3-year old cold production well in the Lloydminster field. The main changes in the reservoir are the pressure dropping from 3000 to 1500 *kPa*, the oil saturation decreases by 10% to 70%, and the solution gas increases to 10% from non-gas in the initial reservoir. These parameters will be applied to the calculations of foamy oil effects on seismic properties.

Table4.1 In-situ reservoir parameters of a 3-year old cold production reservoir

	pre production	post production
Vp (m/s) from logs	2795 m/s	unknown
Vp/Vs (from PikesPeak logs)	1.9	unknown
density from log (g/cm^3)	2.16	unknown
density of grain sand (g/cm^3)	2.65	2.65
oil API	11.3	11.3
specific gravity of methane	0.56	0.56
gas pseudocritical temperature (F)	-116.5	-116.5
gas pseudocritical pressure (Psi)	667	667
solution Gas-Oil ratio	7.5	7.5
reservoir temperature (C)	20	20
reservoir pressure (kPa)	**3000**	**1500**
water saturation (%)	20	20
oil saturation (%)	**80**	**70**
gas saturation (%)	**0**	**10**
water salinity (ppm)	44000	44000
porosity (%)	**30**	**30**

During heavy oil cold production, reservoir sands are transported to the surface. The sand extraction enhances the oil recovery. Figure 4.1 shows that the sand production rate is relatively high during the first few months of the production. After that, the oil production dominates the total production, and the sand production rate tends to be low and stable, but continues throughout the whole production process. In reality, Sawatzky believes that the average porosity within the drainage area will slightly increase, depending on the accumulative production of sands.

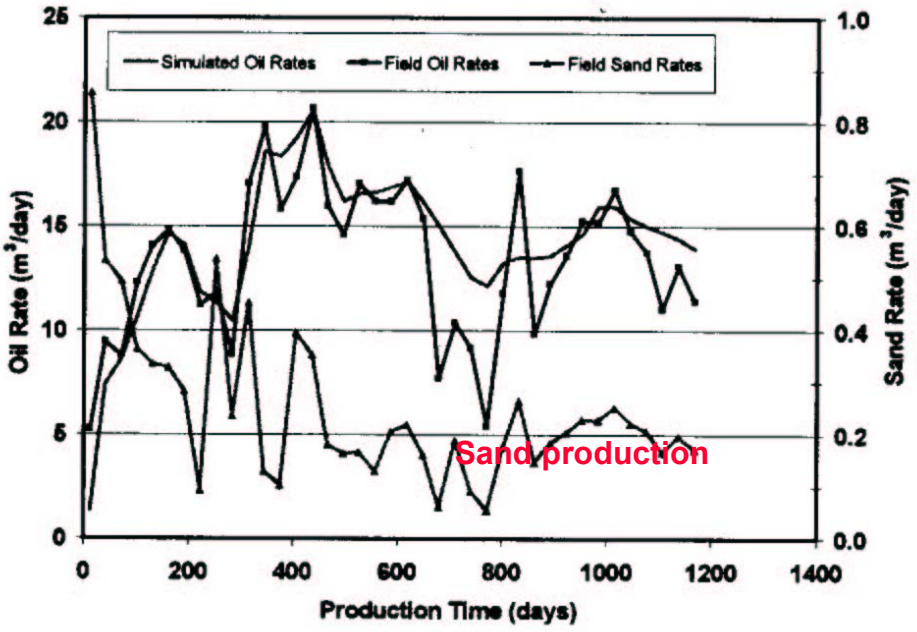

Figure 4.1 Sand production versus heavy oil production in a Lloydminster field (after Sawatzky, et al. 2002)

4.2 Foamy oil effects on seismic properties

In order to better understand the foamy oil effects on seismic properties, we assume that there is no sand extraction during production, which involves only pressure depletion and gas coming out of solution from live heavy oil, leading to the formation of foamy oil. With the presence of foamy oil, the reservoir fluid phases have changed into water, heavy oil and solution gas, from the initial fluid states of water and heavy oil only. With mixed fluid saturations, Gassmann's equation (1951) is employed to calculate the saturated rock bulk modulus K_μ,

$$K_u = K_d + \frac{(1 - K_d / K_s)^2}{\frac{\phi}{K_f} + \frac{1-\phi}{K_s} - \frac{K_d}{K_s^2}}, \tag{4.1}$$

where, the matrix bulk modulus K_s is known as 36 *GPa* for sandstone, and ϕ remains constant during production (no sand extraction). The fluid bulk modulus K_f and the frame bulk modulus K_d are required to be defined before applying the Gassmann equation.

4.2.1 Methodology of computing the frame bulk modulus

The frame bulk modulus K_d can be derived by modifying equation 4.1 as

$$K_d = \frac{1 - (\frac{\phi}{K_f} + \frac{1-\phi}{K_s})K_\mu}{\frac{K_s - K_\mu}{K_s^2} - \frac{\phi}{K_f} + \frac{\phi}{K_s}}, \tag{4.2}$$

where, K_u can be obtained by modifying equations 3.3 and 3.4 as

$$\mu = V_s^2 \rho_\mu , \tag{4.3}$$

$$K_\mu = V_p^2 \rho_\mu - {}^{4\mu}\!/_{3} . \tag{4.4}$$

The *P*- wave and *S*- wave velocities can be obtained from the dipole sonic recorded before the production. Due to the assumption that the average porosity of the reservoir sands remains constant by ignoring sand extraction during production, the frame bulk modulus does not change in both pre- and post-production cases with foamy oil effects only. In the field, the volume of sands is relatively small compared to the total volume of the slurry so that the porosity change is insignificant.

4.2.2 Methodology of computing the mixed fluid bulk modulus

To approximate the bulk modulus of the fluid mixture in a low-seismic frequency range, two kinds of saturations have to be defined; uniform saturation and patchy saturation (Mavko and Mukerji, 1998). With uniform saturation, the mixed fluid bulk modulus is given by

$$\frac{1}{K_f} = \frac{S_g}{K_g} + \frac{S_o}{K_o} + \frac{S_w}{K_w} \tag{4.5}$$

Where, S_g, S_o, S_w and K_g, K_o, K_w are the gas, oil, water saturations and bulk moduli, respectively. This approach is applicable only if the gas, oil and brine phases are mixed

uniformly at a very small scale, so the different wave-induced increments of pore pressure in each phase have time to diffuse and equilibrate during a seismic period.

In contrast, the mixed fluids with a patchy saturation are at a scale that is smaller than the seismic wavelength, but larger than the scale at which the fluids can equilibrate pressures through local flow. The fluid bulk modulus with patchy saturations is given by

$$K_f = S_g K_g + S_o K_o + S_w K_w \quad . \tag{4.6}$$

The effects of mixed fluid bulk moduli with both uniform and patchy saturations are listed in Table 4.2, using the in-situ reservoir parameters in Table 4.1. The results demonstrated that Patchy and Uniform mixture status have dramatically different impacts on the mixed fluid bulk modulus, which could result in strong impacts on rock physical properties discussed later. The computation of the bulk moduli of gas, oil and water, is demonstrated by Batzle and Wang (1992).

Table 4.2 The mixed fluid bulk moduli with Patchy and Uniform fluid mixtures

		P (Kpa)	**Sg (%)**	**Sw(%)**	**So(%)**	**Porosity(%)**	**Kf (Gpa)**
pre-production		3000	0	20	80	30	2.51981
Post-produciton	Patchy mixture	1500	10	20	70	30	2.2455
	Uniform mixture	1500	10	20	70	30	0.0211
	Average						1.1333

Note: *P* is the effective reservoir pressure. *Kf* is the mixed fluid bulk modulus.

4.2.3 Computation of the velocities of saturated sands

Gassmann's equation and equations 3.3 and 3.4 can be applied to calculate the *P*-wave and *S*-wave velocities before and after production. The program used in calculations of bulk and shear moduli and *P*-wave and *S*-wave velocities, is modified from the original program of Zou and Bentley (2002). Figure 4.2 shows that any small amount of gas will cause the estimate of the fluid mixture bulk modulus to be very low with a uniform saturation state, while it only gradually decreases with the increase of gas saturation linearly with a patchy saturation state. The shear moduli with both saturation states do not change because shear waves cannot propagate in fluids. Fgiure 4.3 shows similar results for the *P*-wave and *S*-wave velocities in saturated sands. The *S*-wave velocity increases slightly due to the density decrease. The bulk modulus and *P*-wave velocity of saturated rock are larger if the fluids are "patchy" than if they are uniform. The bulk modulus and velocities with patchy and uniform saturations are defined with Voigt upper bound and Reuss lower bound. Mavko and Mukerji (1998) and Bentley et al, (1999) believe that any moduli and velocities of saturated rock will lie between these two bounds.

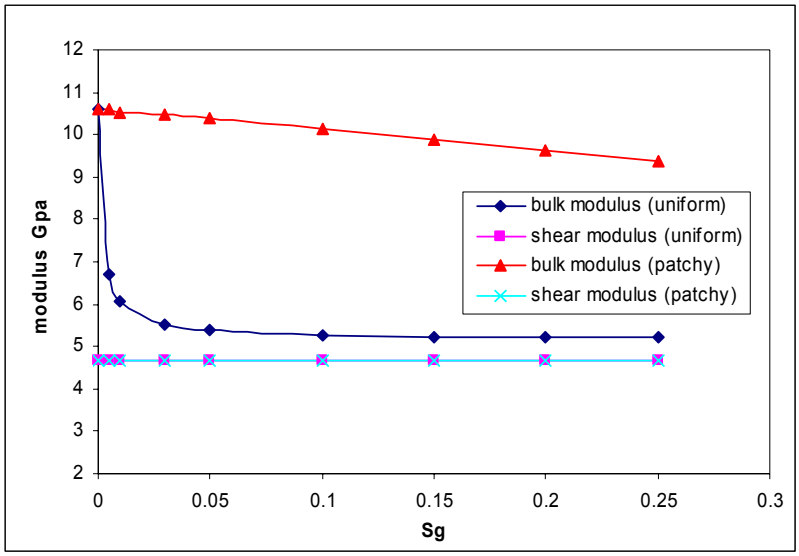

Figure 4.2 The relations of saturated rock bulk modulus and shear modulus with gas saturation changes. Here the reservoir pressure is defined as 3000 *kPa*. K_f is derived from uniform saturation/ Reuss lower bound (Eqn. 4.5) and patchy saturation/Voigt upper bound (Eqn. 4.6) respectively.

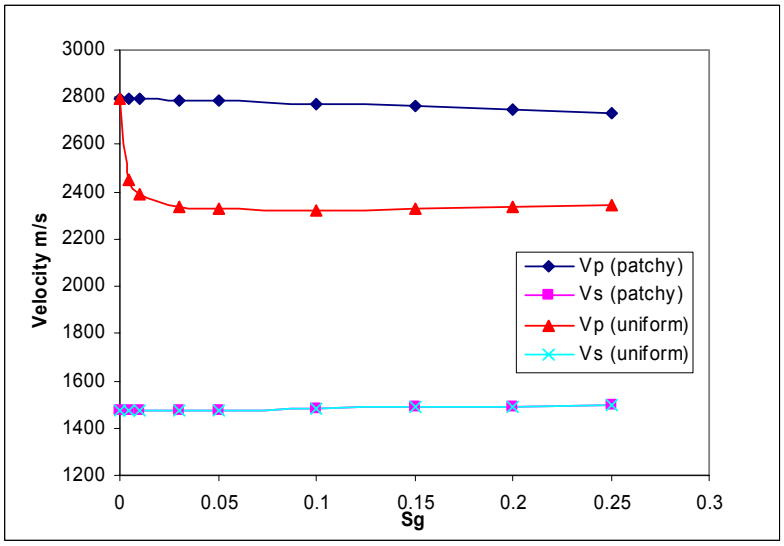

Figure 4.3 The relations of *P*-wave and *S*-wave velocities of saturated rock with gas saturation changes. The results are obtained by applying the data in Figure 4.1.

Table 4.3 contains the physical and seismic properties of reservoir rock in the drainage regions with foamy oil effects before and after production calculated using Voigt and Reuss bounds, as well as the average. With a 10 percent gas saturation, the average bulk modulus of the saturated rock dramatically drops from 10.6*GPa* to 7.8*GPa*, while the shear bulk modulus shows only a slight increase. Hence the average P-wave velocity decreases to 2570*m/s* from 2795*m/s*, and S-wave velocity increases slightly due to the density decrease.

Table 4.3 Siesmic properties of drainage sands with foamy oil effects

physical properties of	pre-production	post-production		
drianage zones with foamy oil effects	Sg=0, So=0.8	Sg=0.1, So=0.7		
		Reuss	Voigt	Average
saturated rock bulk modulus (Gpa)	**10.616**	**5.2252**	**10.113**	**7.807**
saturated shear modulus (Gpa)	4.6726	4.6777	4.6777	4.676
saturated bulk density (kg/m^3)	2156.5	2126.6	2126.6	2126
Vp (m/s)	**2795**	**2325**	**2773**	**2570**
Vs (m/s)	1472	1483	1483	1483

However, due to the lack of data, the actual fluid saturation of the in-situ case is uncertain. It could range anywhere from patchy to uniform saturation states, depending on a host of factors, including gas, oil, and water saturation; relative permeability, fluid density contrast, gravity effects, spatial distribution of permeability, injection rates, and history. Therefore, we assume that the average bulk modulus of the mixed fluids between

patchy and uniform saturations, can better represent the actual fluid bulk modulus. The average values of *P*-wave velocity and density in Table 4.2, will be applied later to the seismic modeling for detecting foamy oil effects.

4.2.4 Effective reservoir pressure effects on seismic properties

Generally, both seismic *P*-wave and *S*-wave velocities increase with the increase of effective reservoir pressure. That's the reason why reservoir pressure changes can be monitored by time-lapse seismic analysis. However, the *P*-wave and *S*-wave velocity variations with pressure are more rapid at high pressure reservoirs as discussed in Chapter 3. For heavy oil cold production reservoir, the effective reservoir pressure varies from 500 *kPa* to 5000 *kPa*. The pressure effects on seismic velocity are reflected through the values of K_g, K_o, K_w using the equations of Batzle and Wang (1992). Figure 4.4 shows that both *P*-wave and *S*-wave velocities are hardly affected by the variations of reservoir pressure at low effective reservoir pressure.

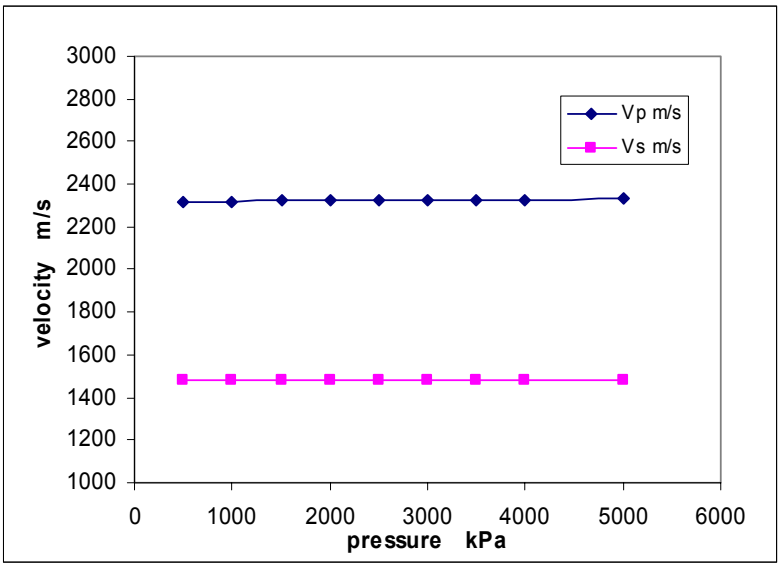

Figure 4.4 *P*-wave and *S*-wave velocity variations with effective reservoir pressure.

4.3 Wormhole effects on seismic properties

4.3.1 Effects of wormhole porosity on seismic properties

As discussed in previous chapters, wormholes develop within the drainage sands that have porosities greater than the critical porosity, where the sands are in fluid-supported state. This character could strongly affect the rock rigidity and physical properties, thus influencing the seismic properties of the reservoir sands based on the theory discussed in chapter 3. Here, the in-situ reservoir parameters have been employed to compute the high porosity effects on seismic velocities and densities of reservoir sands within wormholes.

Again, in this discussion, the foamy oil effects need to be minimized. The results shown the Table 4.3, indicate that the presence of gas hardly affects the saturated rock bulk moduli when using the Voigt upper bound/Patchy mixing state (Eqn. 4.6) to calculate the mixed fluid bulk modulus. Therefore, we employed the Voigt upper bound to calculate the bulk modulus and density of the mixed fluids, which contribute little to the seismic properties of the sands.

Based on the empirical relations from Murphy et al. (1993) and both lower and upper bounds discussed in Chapter 3 (Equations 3.9, 3.12-3.13, 3.15-3.16), the in-situ parameters from the Lloydminster heavy oil field, listed in Table 4.1 have been used to compute the bulk modulus, shear modulus, and seismic velocities of saturated sands corresponding to various porosities. The results of both bulk and shear moduli are illustrated in Figure 4.5. For porosities less than the critical porosity, which is 35%, the bulk and shear moduli based on the empirical relations linearly lie between the lower and upper bounds. The moduli increase rapidly from the suspension value at the critical porosity toward the mineral value at zero porosity. For porosities greater than the critical

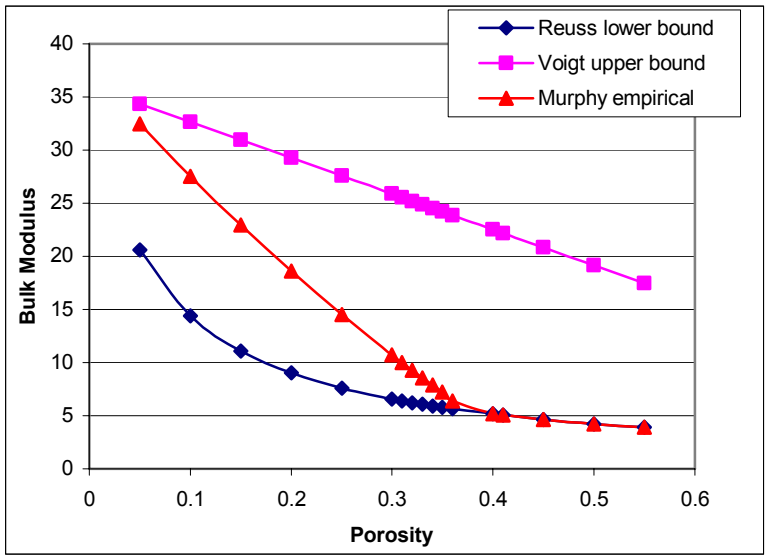

(a)

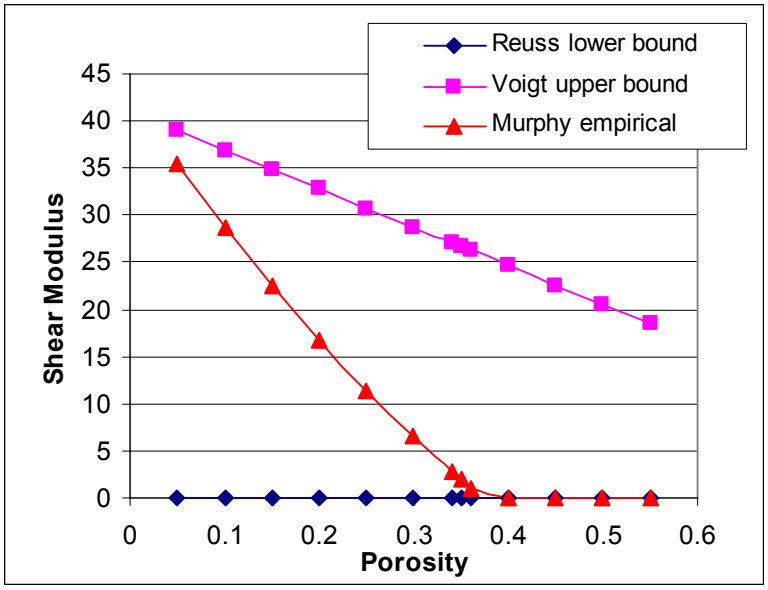

(b)

Figure 4.5 Bulk modulus (a) and shear modulus (b) versus porosity using lower and upper bounds, empirical relations. The critical porosity is 35% approxmately.

porosity, the moduli fit the Reuss lower bound. The shear moduli tend to be zero when grains are suspended in the fluid (Figure 4.5b).

Table 4.4 Seismic velocities versus porosity under the influence of patchy fluid mixture using Murphy's empirical relations

porosity (100%)	Vp (m/s)	Vs (m/s)	Vp/Vs
0.05	4799.5	3719.9	1.29
0.1	4453.9	3407.4	1.31
0.15	4083.2	3068.5	1.33
0.2	3678.8	2694.1	1.37
0.25	3228.7	2267.5	1.42
0.3	**2711.0**	**1752.3**	**1.55**
0.31	2596.0	1631.7	1.59
0.32	2476.0	1502.1	1.65
0.33	2350.3	1361.0	1.73
0.34	2217.8	1204.5	1.84
0.35	2078.5	1038.7	2.00
0.36	1895.3	762.4	2.49
0.4	1645.6	221.5	7.43
0.41	1626.2	162.6	10.00
0.45	1580.7	47.3	33.44
0.5	**1545.0**	**10.1**	**152.96**
0.55	1518.7	2.2	702.84

The empirical relations derived by Murphy et al. (1993) properly fit both lower and upper bounds. We applied them to the calculation of both *P*-wave and *S*-wave velocities with variation of the porosity. The results are listed in Table 4.4 and Figure 4.6. In Figure 4.6, it can be clearly seen that both *P*-wave and *S*-wave velocities decrease with an increase in porosity. The *S*-wave velocity could tend to be zero when porosities are greater than the critical porosity.

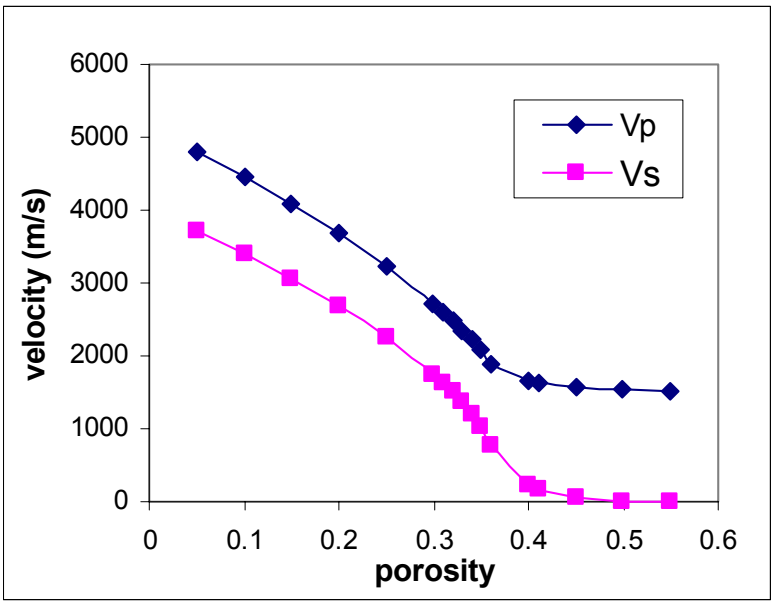

Figure 4.6 *P*-wave and *S*-wave velocities versus porosity using Murphy's empirical equations (Chen et al., 2004)

In the heavy oil cold production case, most of reservoir sands have porosities around 30%, with *P*-wave and *S*-wave velocities of 2711 m/s and 1752 m/s, respectively. However, porosities of wormhole sands are greater than the critical porosity, around 50%. The *P*-wave and *S*-wave velocities of the reservoir sands within wormholes decrease to 1545 *m/s* and 10 *m/s*. The V_p/V_s ratios increase dramatically when porosities are larger than the critical porosity. This is shown in Figure 4.7.

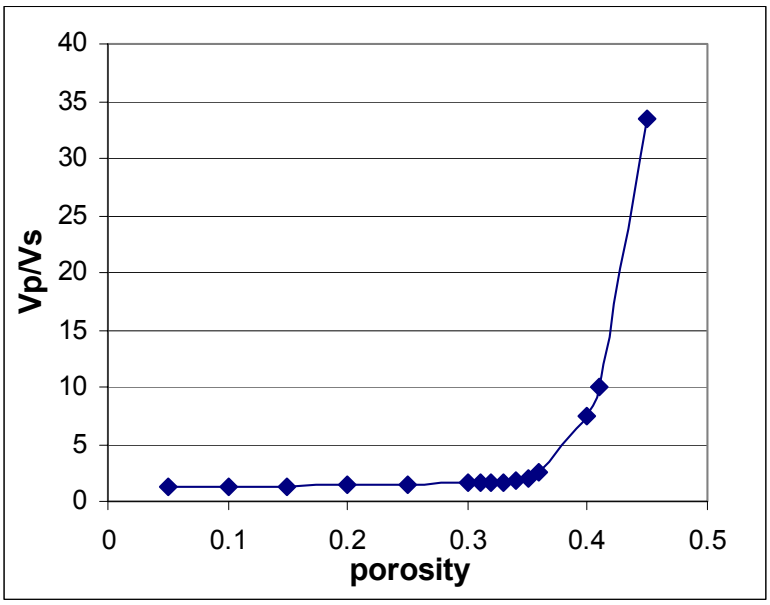

Figure 4.7 *P*-wave and *S*-wave velocity ratios versus porosities from Figure 4.6

4.3.2 Cumulative effects of wormholes on average velocities of drainage sands

Although the presence of wormholes strongly decreases the velocities of sands within wormholes, it is hardly possible for us to detect individual wormholes using surface seismology techniques. High frequency data would be required to image individual wormholes, with a size on the order of centimetres. However, amplitude anomalies have been observed on time-lapse seismic survey from cold production field and it is unclear whether it is due to the foamy oil or wormhole effects, or both. (Mayo, 1996). This indicates that the macroscopic effects of nature of the individual wormholes can be detected, especially when large amounts of sands are extracted from the reservoir.

We believe that the amplitude anomalies seen on time-lapse seismic data can represent the cumulative effects of wormholes.

However, the average effects of wormholes on the velocities of reservoir sands, are strongly dependent on the density of wormholes within the drainage pay zone, where most of sands are extracted. Here, the density of wormholes φ is defined as the percentage of wormhole volume over the total volume ratio of the drainage zone based on our heavy oil cold production model (Figure 2.1). Therefore, the wormhole effects on the velocities of the reservoir sands are limited to the drainage zone, and the effects are also wormhole density dependent. Outside of the drainage zone, the reservoir sands are undisturbed.

It is necessary that some manner of defining the average *P*-wave, *S*-wave velocities (V_p and V_s), and density ρ of the drainage zones be adopted. Here, we assume that the drainage sands consisting of two phases, including the saturated sands and wormhole sands, with porosities of 30% and 50%, respectively. Based on the concept of Reuss lower and Voigt upper bounds, we modified the two equations 3.15 and 3.16 to yield:

$$\frac{1}{V_R} = \frac{1-\varphi}{V_{sat}} + \frac{\varphi}{V_{wm}}, \tag{4.7}$$

Where, V_R is the lower bound of the average velocity in the drainage zone.

$$V_V = (1-\varphi)V_{sat} + \varphi V_{wm}, \tag{4.8}$$

Where, V_v is the upper bound of the average velocity in the drainage zone. V_{sat}, V_{wm}, φ are the velocities of saturated initial reservoir sands and wormhole sands, as well as the wormhole density. The average velocities of the drainage sands influenced by the wormholes will lie between the two bounds.

The average velocities of the drainage sands versus wormhole density changes have been shown in Figure 4.8, using both Reuss Lower and Voigt Upper Bounds and the average of both bounds. In the calculation, the *P*-wave and *S*-wave velocities of the reservoir sands and wormhole sands are obtained from Table 4.4 at porosities of 30% and 50%, respectively. The density of the wormholes range from 0% to 24% of the total reservoir volume.

In Figure 4.8, both *P*-wave and *S*-wave velocities decrease with an increase of wormhole density. *P*- wave velocities seem to have linear relations with the variation of wormholes density using both bounds. The *S*-wave velocities trend to a linear relation with wormhole density using the upper bounds, while being nonlinear using the lower bound. It can be observed that V_s decreases significantly even with 2% of wormholes

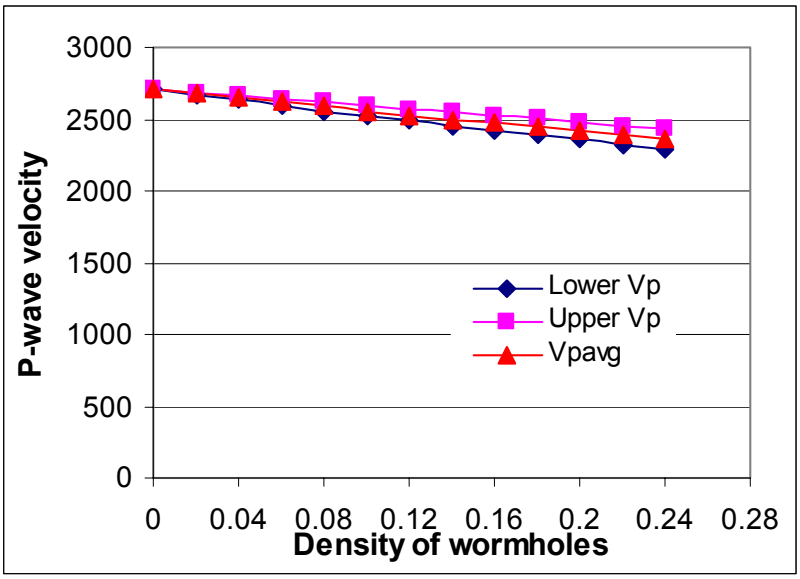

(a)

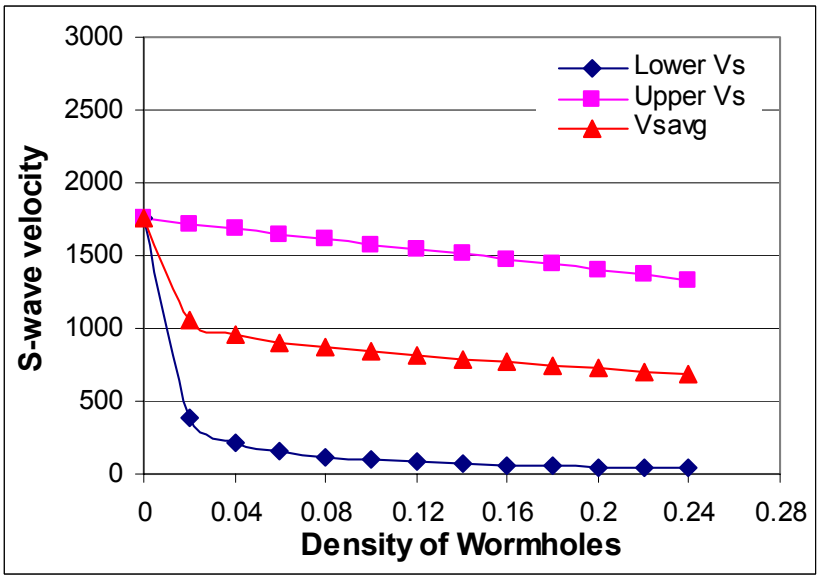

(b)

Figure 4.8 *P*-wave (a) and *S*-wave (b) velocities versus wormhole density using the lower and upper bounds, as well as the average.

within the drainage zone using the lower bound. However, in reality, a small amount of wormholes could not significantly change much the rigidity of the sands. In other words, with a small percentage of wormholes, the sands could be still stiff, and the rigidity changes would be proportional to the wormhole density. Therefore, we think that the upper bound may be more reasonable to describe the average velocity of the drainage sands with wormhole influence. Table 4.5 lists the V_p and V_s, as well as bulk density of the drainage region with the changes of wormhole density.

Table 4.5 Seismic velocities versus wormhole density under the wormhole effects with the Patchy fluid mixture using the Voigt Upper bound

wormhole density (100%)	Vs (m/s)	Vp (m/s)	density (kg/cm^3)	Vp/Vs
0	1752	2711	2126.6	1.55
0.02	1717.16	2687.68	2119.6	1.57
0.04	1682.32	2664.36	2112.6	1.58
0.06	1647.48	2641.04	2105.7	1.60
0.08	1612.64	2617.72	2098.7	1.62
0.1	1577.8	2594.4	2091.7	1.64
0.12	1542.96	2571.08	2084.7	1.67
0.14	1508.12	2547.76	2077.8	1.69
0.16	1473.28	2524.44	2070.8	1.71
0.18	1438.44	2501.12	2063.8	1.74
0.2	1403.6	2477.8	2056.8	1.77
0.22	1368.76	2454.48	2049.8	1.79
0.24	1333.92	2431.16	2042.9	1.82

Figure 4.9 demonstrates the change rate of V_p, V_s, and ρ of the drainage sands with wormhole effects, compared with that of the initial reservoir sand. The density changes are minor with the increase of wormhole density. But it clearly shows that the variations of V_p and V_s increase with the increase of wormhole density in linear relations. The changes of *S*-wave velocity seem much more sensitive to the presence of wormholes than does the *P*-wave. Therefore, converted waves may better image the cumulative effects of wormholes on seismic data.

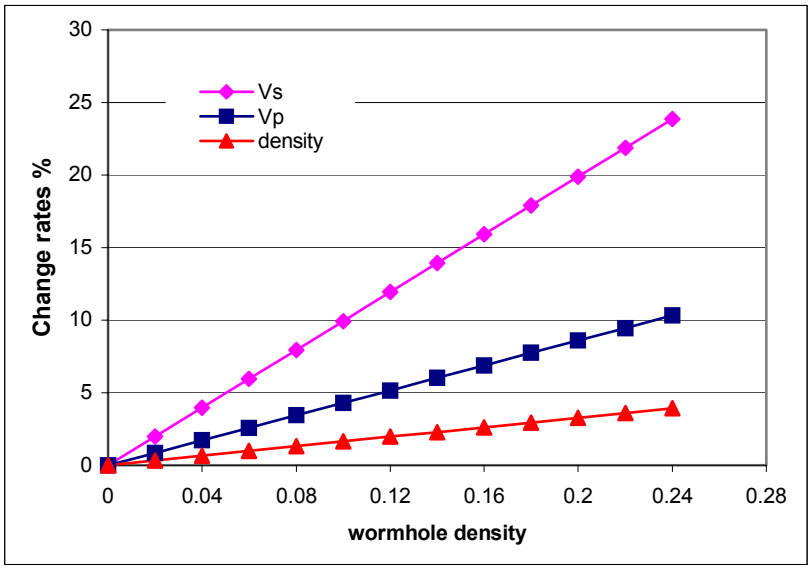

Figure 4.9 The variation rates of *P*-wave and *S*-wave velocities, and bulk density with the increases of wormhole density using the Upper bound equation

4.4 Chapter summary

Based on the results from fluid substitutions and reservoir pressure changes, we observed that foamy oil effects on both *P*-wave and *S*-wave velocities and bulk density are mainly due to the solution gas exolving into the heavy oil because of pressure reduction during cold production. The presence of gas, even a small amount, can significantly reduce the *P*-wave velocity, and slightly decrease the bulk density, while doing little to the *S*-wave velocity. Therefore, the presence of foamy oil should only be detected on *PP* seismic data (Chen, et al., 2004).

However, the presence of wormholes could decrease not only the *P*-wave velocity but also the *S*-wave velocity of the drainage sands. Further, the changes of the *S*-wave velocity vary more rapidly than that of the *P*-wave velocity. That could result in better image of wormhole effects on the *PS* seismic data (Chen, et al., 2004).

According to our geological model (Figure 2.1), the distribution of wormholes likely grows in a radial pattern around the borehole. The distribution of wormholes in the drainage zone may not likely be homogenous or symmetric around the borehole. Instead, they could likely grow along certain geological sand trends in the reservoir. Based on the field observations, we believe that most of the wormholes extend in a certain orientation

within the reservoir, with a variation of wormhole densities, high near the borehole and low away from the borehole. Therefore, the seismic amplitude changes caused by wormhole density variations, could correspond to the wormhole distribution pattern. Basically, the greater the V_p and V_s changes, the stronger the amplitude anomalies will appear. This way we could image the drainage pattern in the reservoir and detect the most likely orientations of wormhole growth using both *PP* and *PS* seismic data.

CHAPTER 5: Time-lapse seismic modeling on foamy oil and wormhole models

In this chapter, numerical seismic modeling will be conducted to observe the seismic responses of foamy oil, wormholes, as well as the combined responses of foamy oil and wormholes. These results will be compared and analyzed to determine which factor could cause stronger impacts on seismic data, and can be applied to imaging the cold production footprints using time-lapse techniques.

5.1 Seismic modeling of foamy oil effects

Here, only the foamy oil effects on seismic responses are discussed. In other words, the effects of wormholes on reservoir properties are ignored. The geological model in Figure 2.1 has been modified as shown in Figure 5.1, where the reservoir state of post-production has been changed to heavy oil, water and foamy oil with gas bubbles within the drainage zone, comparing with the initial reservoir state of heavy oil and water only. Again, the sand extraction has been ignored.

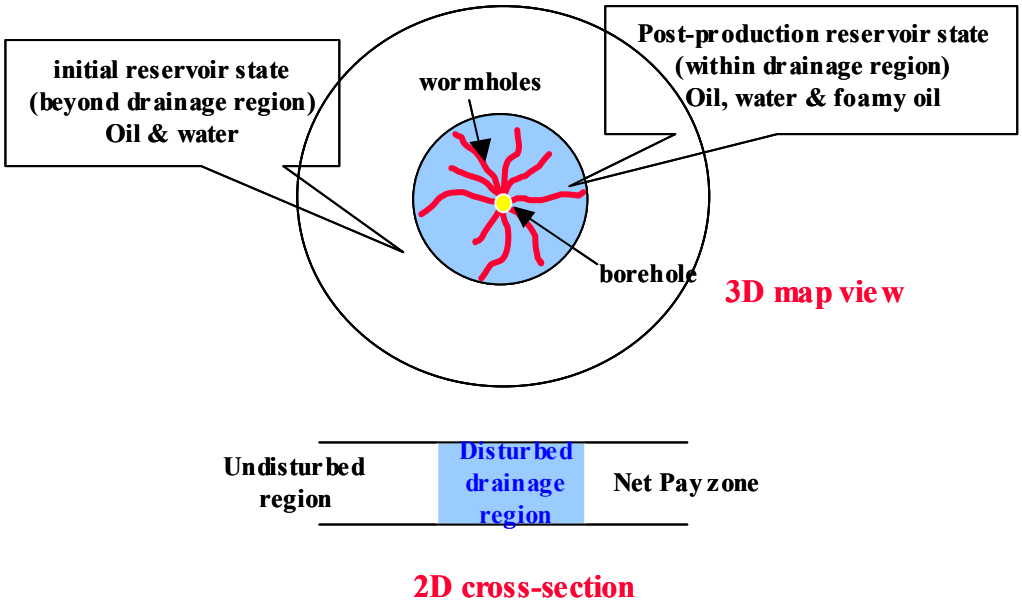

Figure 5.1 Simplified drainage model of cold production reservoir, with a disturbed drainage zone full of foamy oil only (modified from Figure 2.1).

5.1.1 Foamy oil numerical/velocity model

Before production, the initial geological 2D model was built based on the logs from one well drilled by EnCana Corporation in the Lloydminster heavy oil cold production pool. The production zone is the McLaren Formation consisting of unconsolidated sandstones in the Upper Mannville BB Pool. According to the density, gamma ray and *P*-wave velocity (converted from sonic) logs, a geological model of the initial reservoir has been built and is shown in Figure 5.2. This model is 1000 meters in length and depth, consisting of four layers matching the variations of well logs. From top

to bottom, layer 1 is defined from the surface to the top of Mannville Formation at 726*m* with a *P*-wave velocity of 2496*m/s* and a density of 2.26g/cm^3; layer 2 is from the top of Mannville Formation to the top of the McLaren Formation at 742*m* with a *P*-wave velocity of 3227*m/s* and a density of 2.37g/cm^3; layer 3, the production formation, with a *P*-wave velocity of 2795*m/s* and a density of 2.16g/cm^3, is from the top of McLaren Formation to 760*m*, rather than the bottom of the McLaren Formation. The reason for this is because there are sharp variations in both density and velocity logs at the bottom of Maclaren Formation, which are probably due to the highly cemented sand. Layer 4 is from 760*m* to the bottom of the model at 1000*m* with a *P*-wave velocity of 3261*m/s* and a density of 2.4g/cm^3. The interval velocities and densities of each layer except layer 4 are calculated from logs corresponding to their depths. The interval velocity and density of layer 4 are the averages from 760*m* to 800*m* on the logs.

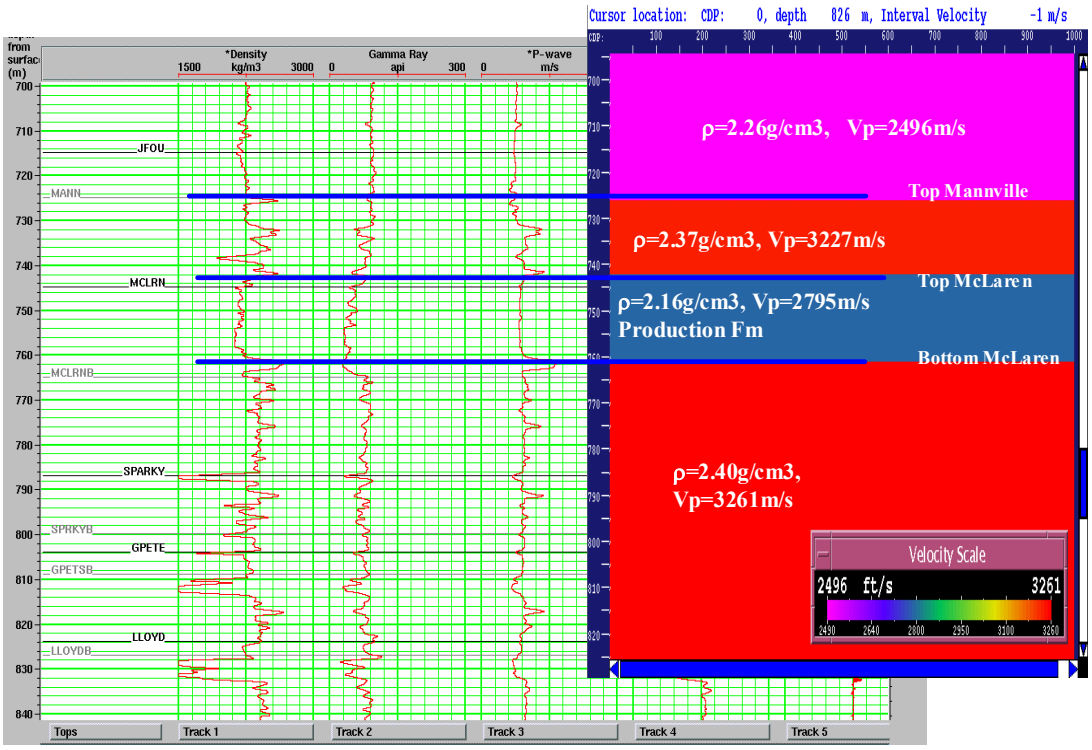

Figure 5.2 The initial reservoir model based on a Lloydminster cold production well. Oil is produced from the Mclaren Formation. The numerical model is 1000*m* in both length and depth, containing 4 layers. The initial *P*-wave velocities and densities are obtained from the well logs.

From the porosity, gamma ray and resistivity logs (shown in Figure 5.3), we can see that there are two main preferred pay zones in the MacLaren Formation based on the high porosity and resistivity characteristics. One is from 745*m* to 750*m* and the other from 755*m* to 758*m*. During production, these two pay zones were perforated and oil was produced from there. That is also where the reservoir was depleted and drained with

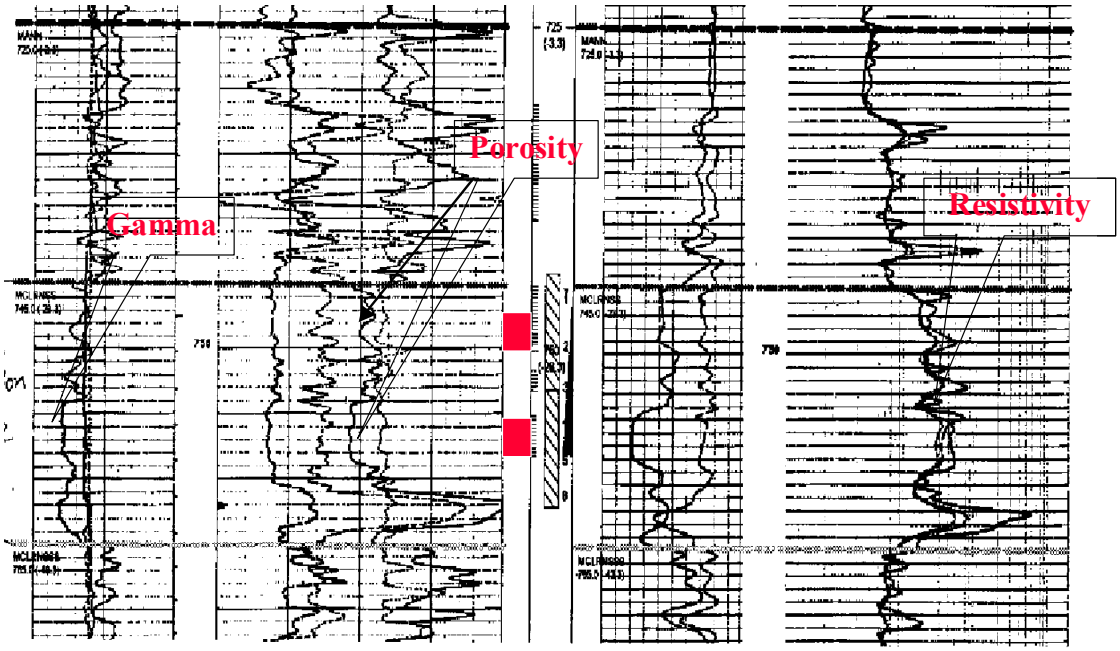

Figure 5.3 Two most likely pay zones (5*m* thick above, 3*m* below in red) shown on the porosity and resistivity logs from the same well as in Figure 5.2, where the formation was perforated and likely depleted and drained.

the decrease of reservoir pressure, resulting in the formation of foamy oil with gas bubbles. At the same time, sands were extracted and wormholes would likely have developed within the two pay layers. Assumed that the diameters of the drainage region will extend 200*m* and 300*m* respectively, through the entire pay zones due to the growth of wormholes, where the reservoir pressure decreases. Therefore, based on the geological cylinder model, a 2D post-production drainage model with foamy oil effects has been

built, consisting of the two drainage regions in the Mclaren Formation around the well in the middle of the model (Figure 5.4).

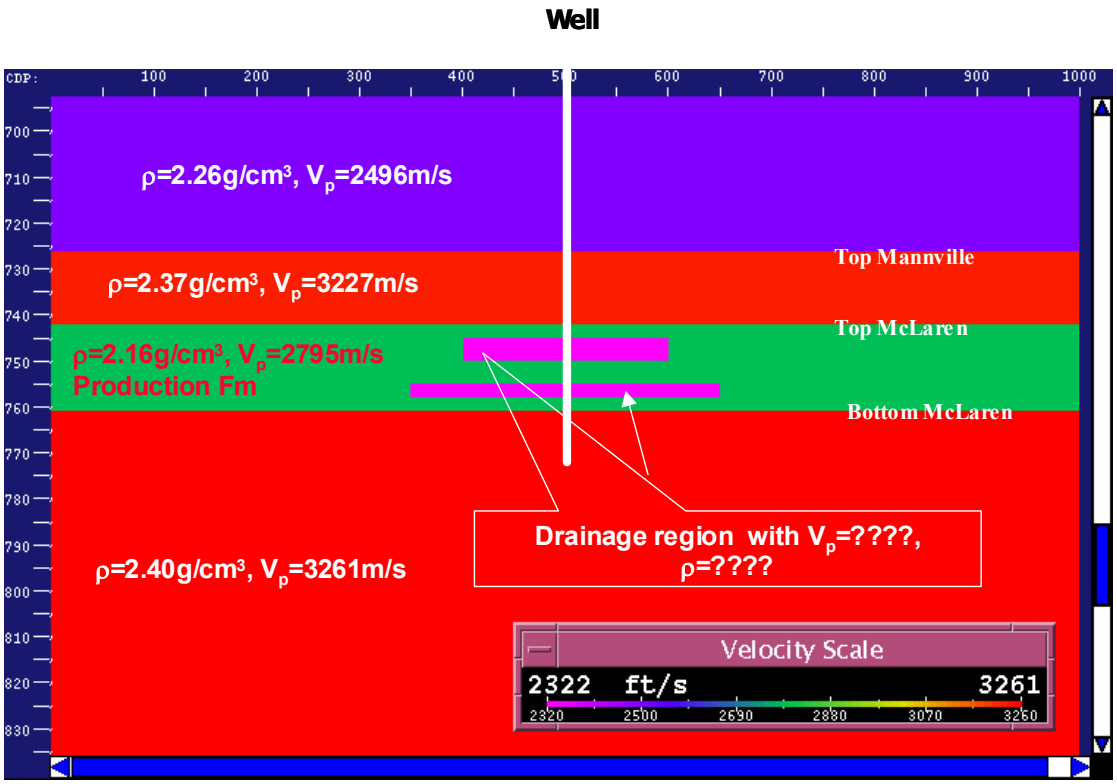

Figure 5.4 Post-production numerical model of the initial model in Figure 5.2 with foamy oil effects only. Two drainage regions are defined as 5*m* and 3*m* thick, and 200*m* and 300*m* in length, respectively (Chen, et al., 2004).

The next question is to determine the velocities and densities within the drainage regions. Based on the in-situ calculations in chapter 4, Table 4.2 illustrates the velocities and density under the influences of the foamy oil using different fluid mixture

mechanisms. In this model, we employ the average values of both Reuss and Voigt bounds. Therefore, with the foamy oil effects only, the *P*-wave velocity decreases to 2570*m/s* from the initial velocity of 2795*m/s,* the density changes to 2.13g/cm^3 from 2.16 g/cm^3, and the *S*-wave velocity slightly increases due to the decrease of the bulk density, but changes minimally from the initial value because *S*-waves cannot propagate through the fluid. The post-production numerical model with foamy oil effects is demonstrated in Figure 5.5.

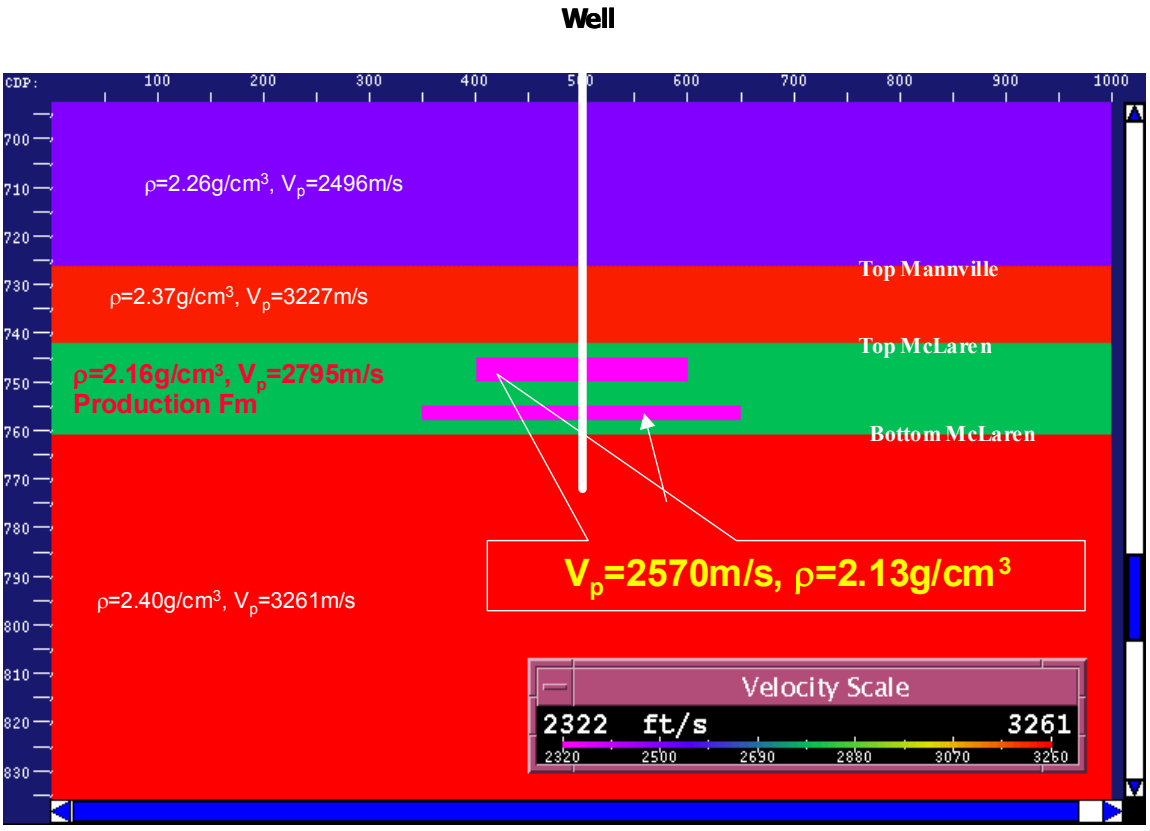

Figure 5.5 Post-production numerical model with foamy oil effects

5.1.2 PP seismic data modeling and results

Based on the pre- and post-production numerical models shown in Figure 5.2 and 5.5, zero-offset seismic traces with and without drainage regions were generated using Finite Difference Method. Kirchhoff depth migration was then applied using the module in the Promax software package. The velocity and density grid is 1m by 1m. CDP intervals are 1m. Figure 5.6 illustrates the migrated sections of pre- and post-production models. As well, the difference between the two seismic sections at a frequency bandwidth of 5 - 200Hz is shown. Here we can observe the amplitude anomalies and traveltime delays caused by the two drainage regions, with lower *P*-wave velocity and density compared with the ambient rocks. In Figure 5.6 (c), the negative amplitude anomalies are obvious and indicated in yellow around 750 meters. The size of the anomalies is indicative of the two drainage regions. In Figure 5.6 (d), the difference of sections (b) and (c) shows the strong amplitude anomalies and traveltime delays below the anomalies, caused by the lower velocity and density within the two drainage zones.

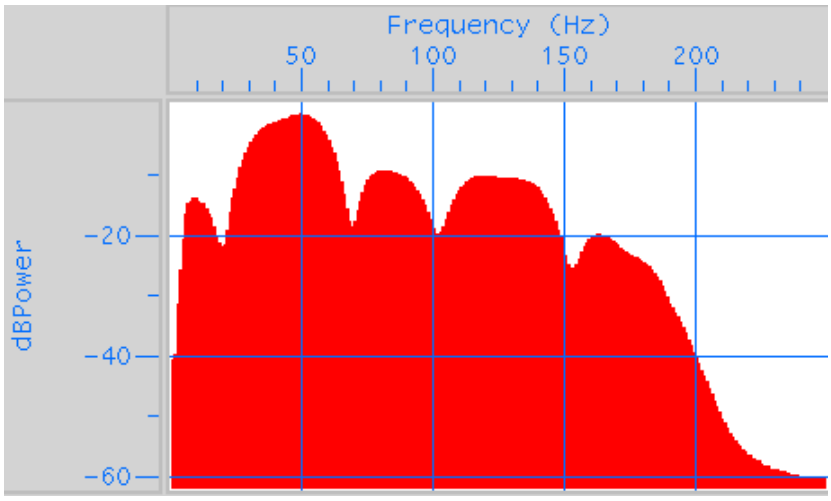

(a) a zero-phase wavelet with a frequency bandwidth of 5-200*Hz*

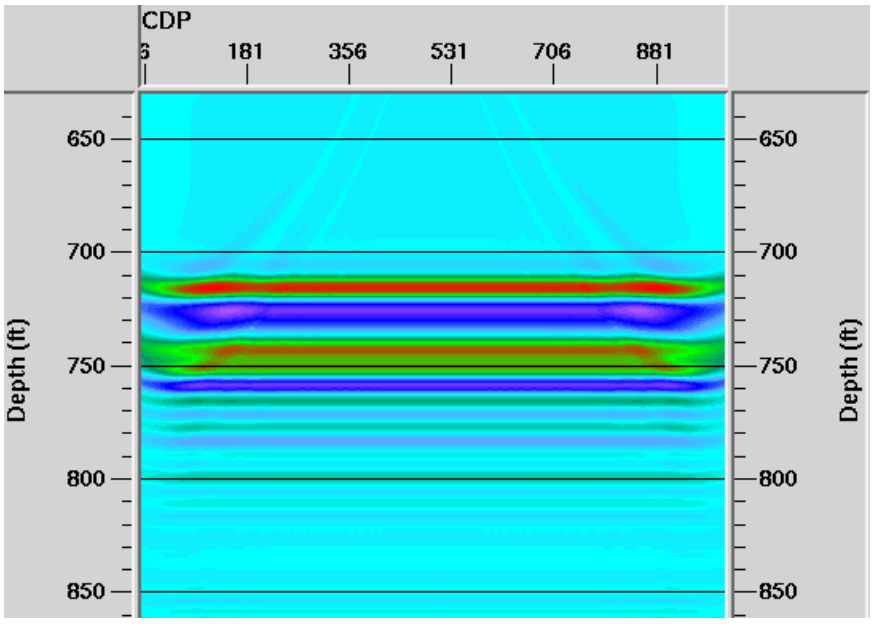

(b) Seismic response of pre-production model in Figure 5.2

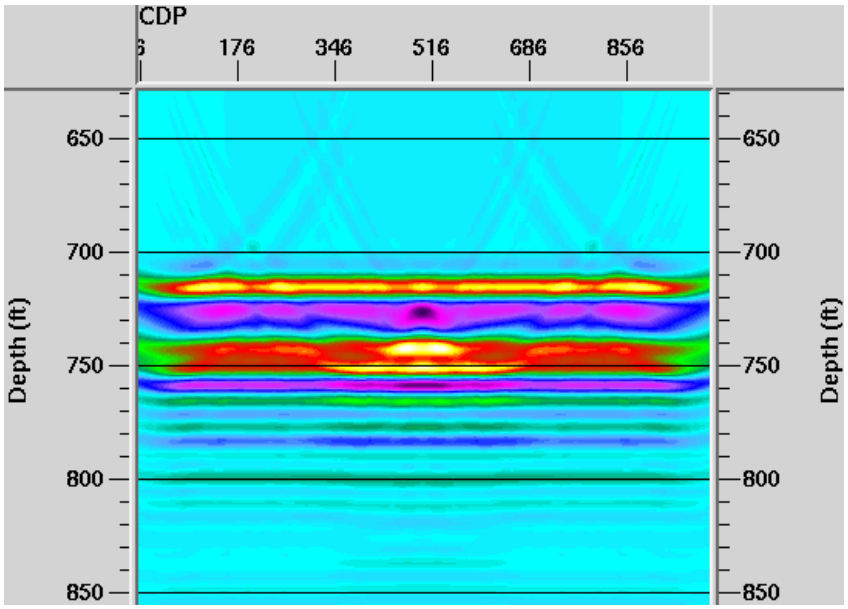

(c) Seismic response of post-production model in Figure 5.5

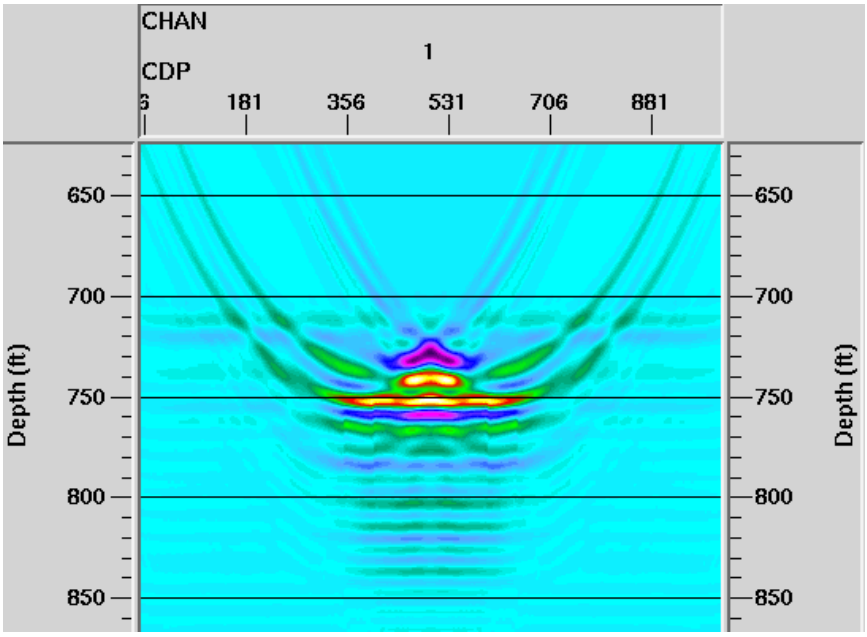

(d) The difference of pre- and post-production seismic responses

Figure 5.6 Migrated seismic sections of pre- and post-production models with foamy oil effects at a 5 – 200*Hz* frequency bandwidth (Chen, et al., 2004).

Upon changing the upper frequency in the bandwidth to 100*Hz* and 50*Hz*, seismic responses can only show the cumulative responses of the two drainage regions (shown in Figure 5.7-5.8). Comparing with Figure 5.6, where the two drainage regions are clearly separated, Figure 5.7 only can illustrate a cumulative image of the two drainage regions. Meanwhile, the amplitude anomaly is almost totally blurred in Figure 5.8 with a 50 *Hz* frequency.

Considering these drainage regions as thin beds, the clear and detailed images of the amplitude anomalies corresponding to the drainage regions are determined by the seismic vertical resolution, which is related to the velocity of the drainage region and the frequency bandwidth. In our case, the highest vertical resolution is about 2.9*m* with a frequency bandwidth of 200*Hz*. That is the reason why we can distinguish these two drainage regions in Figure 5.6. We believe that the seismic frequency bandwidth plays an important role in detecting the image of the drainage regions. For our model, the Fresnel zone, which is much smaller than the diameter of the drainage zone, is not an issue here.

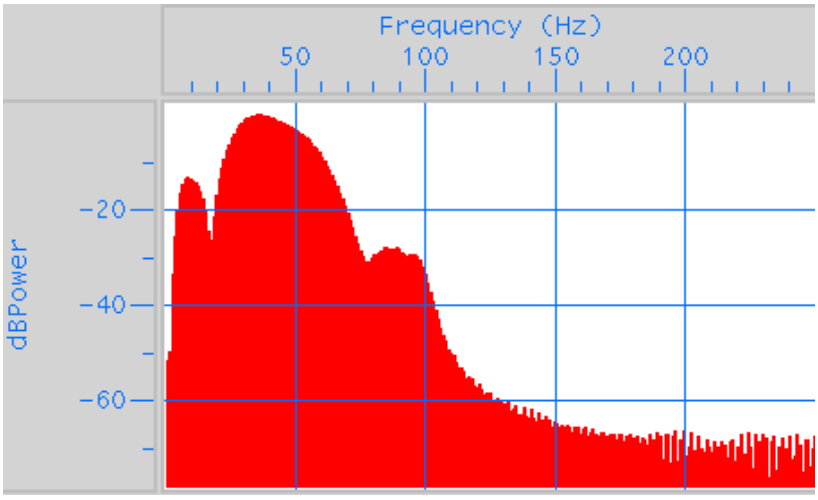

(a) a zero-phase wavelet with a frequency bandwidth of 5-100*Hz*

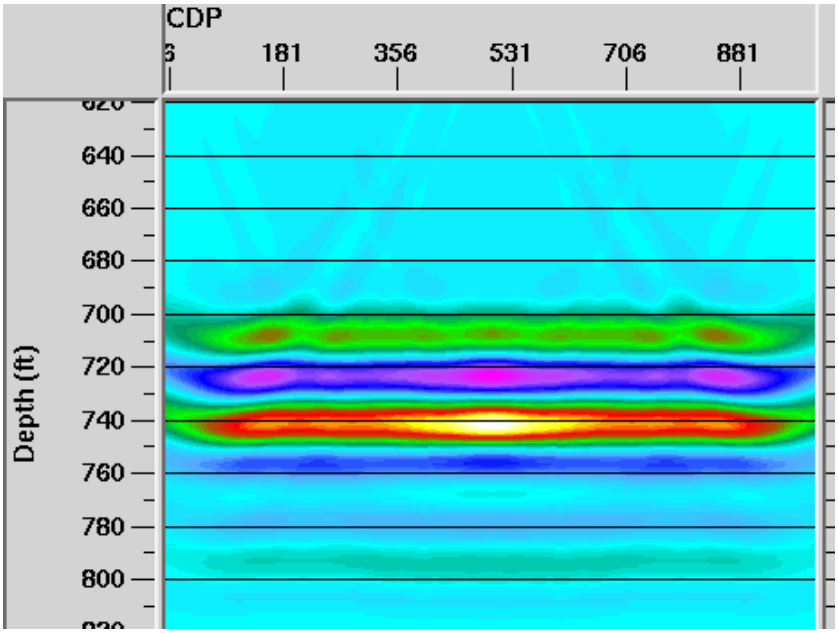

(b) The post-production seismic responses

Figure 5.7 Migrated seismic sections of post-production model with foamy oil effects at a 5 – 100*Hz* frequency bandwidth (Chen, et al. 2004)

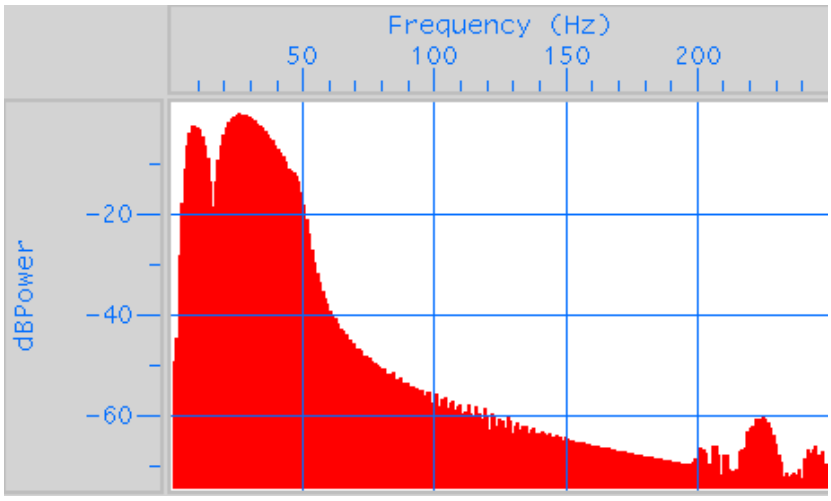

(a) a zero-phase wavelet with a frequency bandwidth of 5-100*Hz*

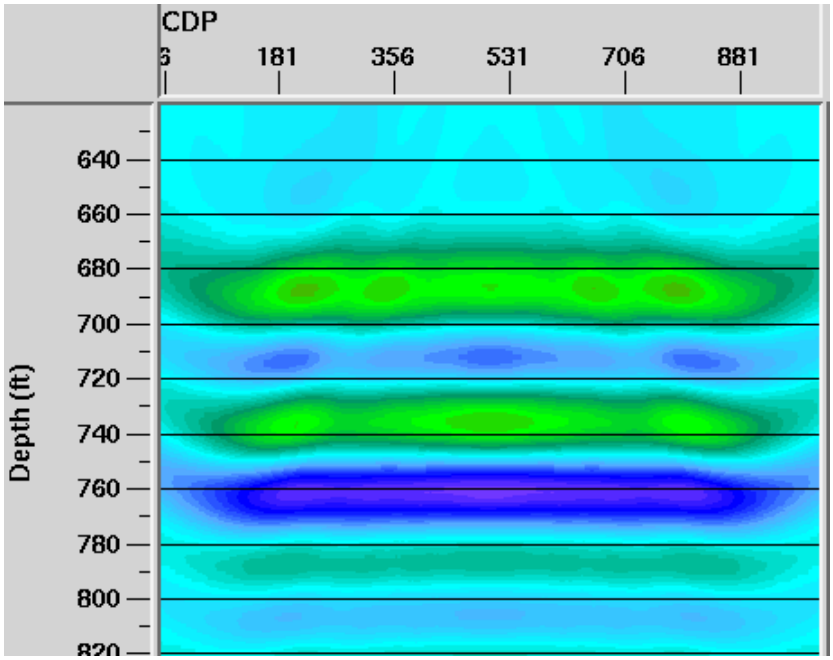

(b) The post-production seismic responses

Figure 5.8 Migrated seismic sections of post-production model with foamy oil effects at a 5 – 50*Hz* frequency bandwidth (Chen, et al. 2004)

5.2 Seismic modeling of wormhole effects

Here, only the wormhole effects on seismic responses are addressed. In order to minimize the foamy oil effects where gas exists within the reservoir, the patchy fluid mixture state is employed to demonstrate the presence of gas, where the influence of gas on the mixed fluid bulk modulus is relatively small based on the calculation shown in Table 4.2, thus resulting in only slight changes on the velocities and density of the saturated rock (shown in Table 4.3). Therefore, the major impact on the velocity and density of the saturated sands result from the presence of wormholes as addressed in Chapter 4, where sands are produced and the porosity and rigidity of the reservoir sands have changed. The geological model in Figure 2.1 has been modified as shown in Figure 5.9, where the reservoir state of post-production has been highly disturbed with the presence of wormholes.

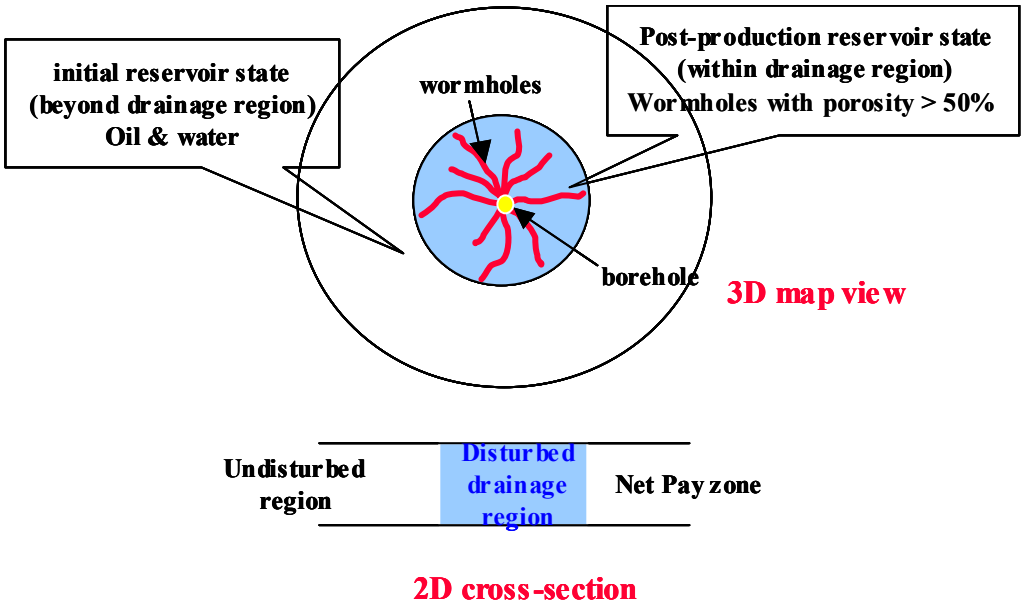

Figure 5.9 Simplified drainage model of a cold production reservoir (modified from Figure 2.1), with a disturbed drainage zone dominated by wormhole effects. Oil, water and foamy oil also exist, but the foamy oil effects have been minimized using the Patchy saturation state.

5.2.1 Numerical/velocity model with wormhole effects

Considering that the net pay thickness of most cold production reservoir are thin, less than 10m, we assume that wormhole effects on rock properties can overwhelm through the entire pay thickness. The pre-production 2D reservoir numerical model is modified from the model in Figure 5.2, consisting of 5 layers instead of 4, in order to better image the traveltime delay. The velocities and densities are listed in Table 5.1.

Figure 5.10 shows the post-production model due to wormhole effects (1000 meter by 1000 meter in depth and width) with one drainage zone, 6*m* thick, and 200*m* long. The drainage zone has been divided into 10 lateral blocks. A wormhole density increase from 2% to 20% in adjacent blocks is incorporated, corresponding to V_p varying from 2688*m/s* to 2478*m/s* and V_s from 1717*m/s* to 1404*m/s* obtained from Figure 4.7 using the Upper bound calculation. The detailed values of the numerical model are listed in Table 5.1. The reason for designing lateral wormhole density change is to observe the variations of amplitude with this change.

Table 5.1 Parameters of the numerical drainage model with wormhole effects only

Initial model parameters				Daiange chambers model parameters			
layers	Vp (m/s)	Vs (m/s)	density (kg/m^3)	chambers	Vp (m/s)	Vs (m/s)	density (kg/m^3)
1	2496	1441	2081	1	2688	1717	2117
				2	2664	1682	2110
2	3227	1863	2219	3	2641	1647	2103
				4	2618	1613	2096
3	2711	1752	2124	5	2594	1578	2089
				6	2571	1543	2082
4	3261	1883	2224	7	2548	1508	2075
				8	2524	1476	2068
5	3500	2021	2264	9	2501	1438	2061
				10	2478	1404	2055

Note: The initial/pre-production model parameters are derived from well logs in Figure 5.2. The drainage chambers from 1 to 10 are corresponding to the wormhole density from 2% to 20%, and the velocities and densities are derived from Figure 4.7 in Chapter 4.

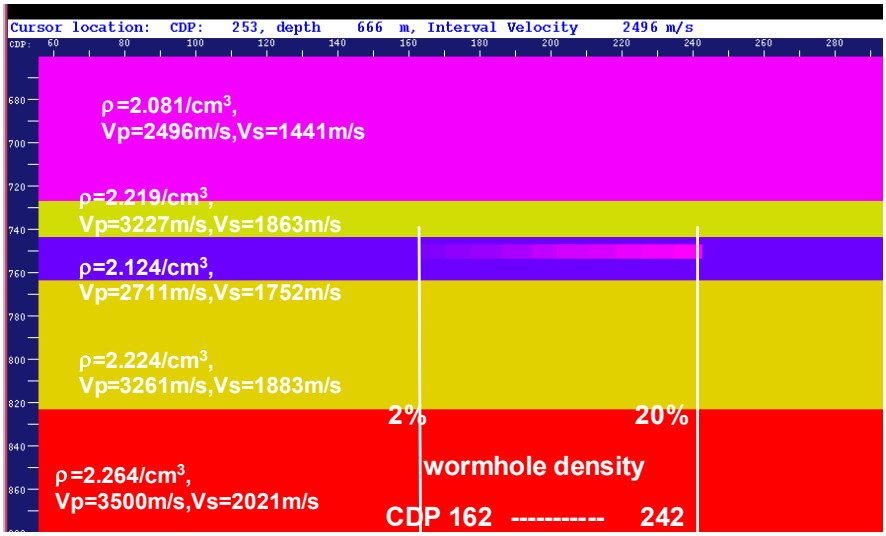

Figure 5.10 Post-production numerical model with wormhole effects

5.2.2 PP and PS seismic data modeling and results

Since the presence of wormholes influences both *P*- and *S* - wave velocities, the seismic survey has been designed to acquire both reflection energy (*PP* wave) and converted energy (*PS* wave). The sources were shot at the free surface with a total of 101 shots at an interval of 10 meters, moving from the left end of the model to the right end at 1000m. The array of receivers is 400-meter long at 5-meter interval, starting at the zero offset, where the shot is located. The array of the receivers moves with the shots. GX 2D ray-tracing modelling has been employed to generate the synthetic shot gathers of *PP* and *PS* data for both pre- and post-production reservoir model with wormhole effects. Both *PP* and *PS* shot gathers have been input into the Promax for stacking. The processing

flow is listed in Figure 5.11. Converting *P*-wave RMS velocity to the RMS velocity of *P*-wave down and *S*-wave up requires the input of the V_p/V_s ratio varying with the depth, which can be derived from the *S*-wave velocity model in GX modeling. The flow of P–S asymptotic binning is to rearrange the bin centres of the *PS* data based on a general V_p/V_s ratio in the model.

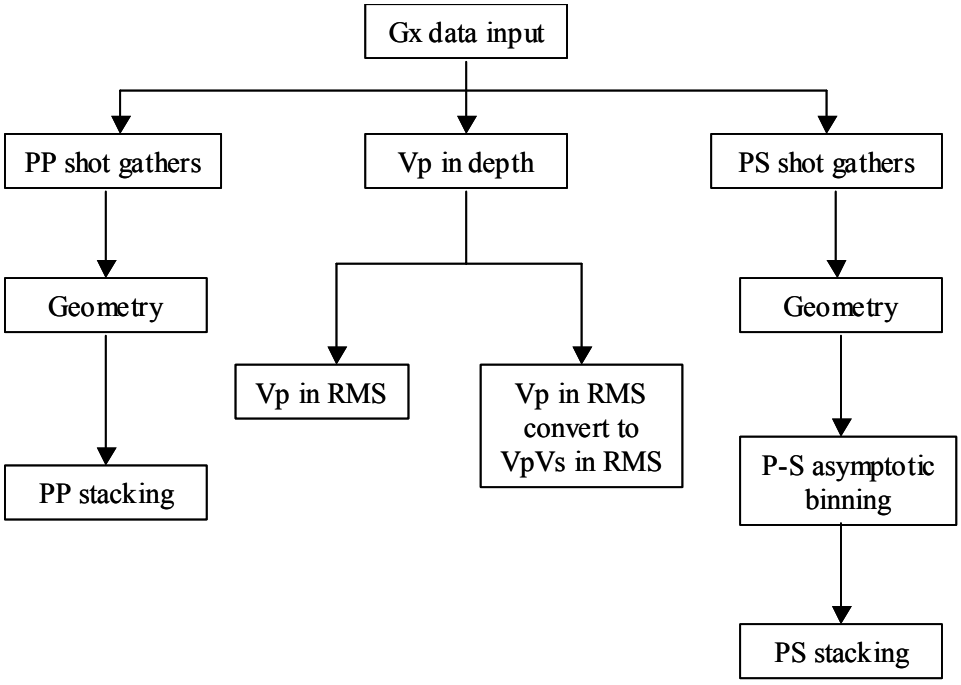

Figure 5.11 The processing flow of stacking *PP* and *PS* data in Promax

Figure 5.12 shows the stacking sections of *PP* seismic data of the pre-production reservoir model and the post-production model with the drainage zone, as well as the difference section by subtracting Figure 5.12a and 5.12b. The wavelet employed here is

zero-phase, 60*Hz* Ricker wavelet. In Figure 5.12b, the drainage zone locates between CDP 162 and 242. Here, slight amplitude and phase changes can be observed within the drainage zone. The changes can be easier seen around CDP 240, where the higher wormhole density of 20% exists, corresponding to larger *P*–wave velocity contrast. The difference of the amplitudes and phases can be clearly observed in Figure 5.12c. Also, the traveltime delay can be observed underneath the high wormhole density zone around CDP 240, due to the lower velocity and density contrasts with higher wormhole density.

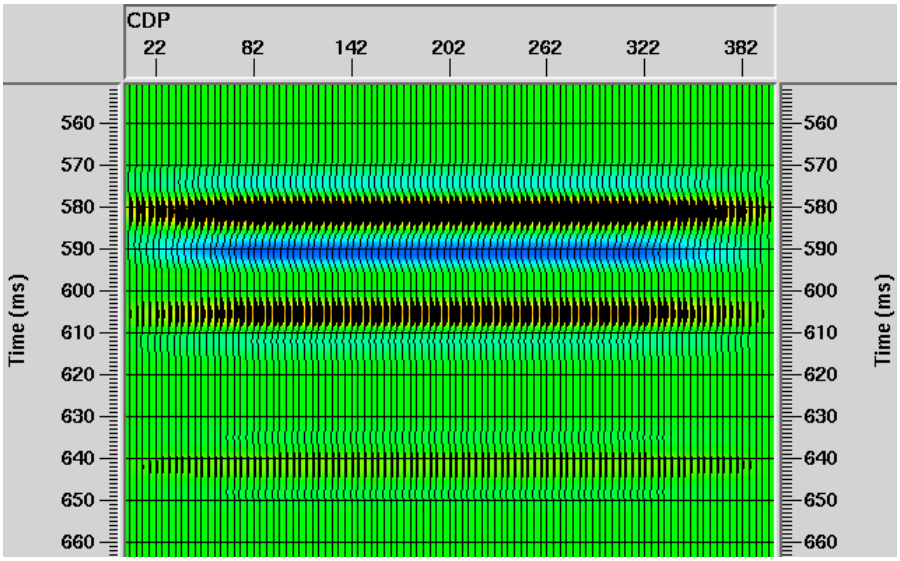

(a) *PP* seismic response of the pre-production model

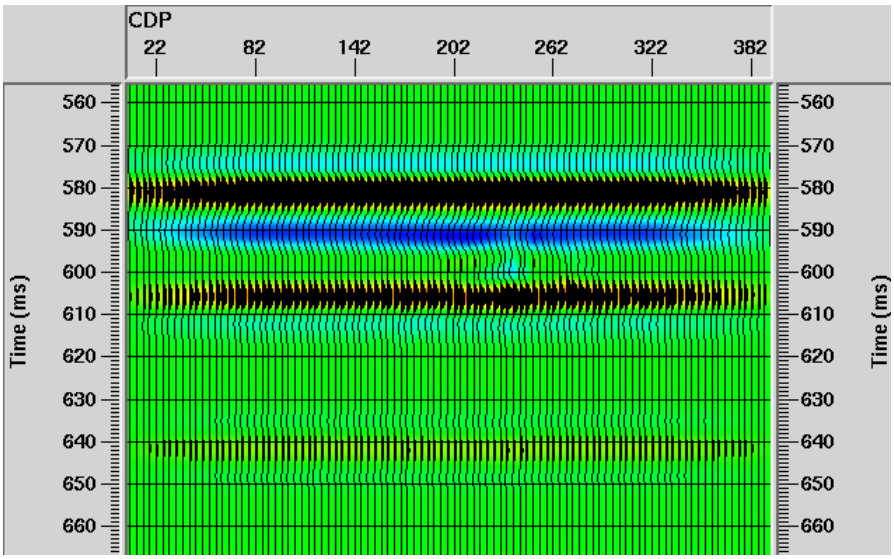

(b) *PP* seismic response of the post-production model in Figure 5.10

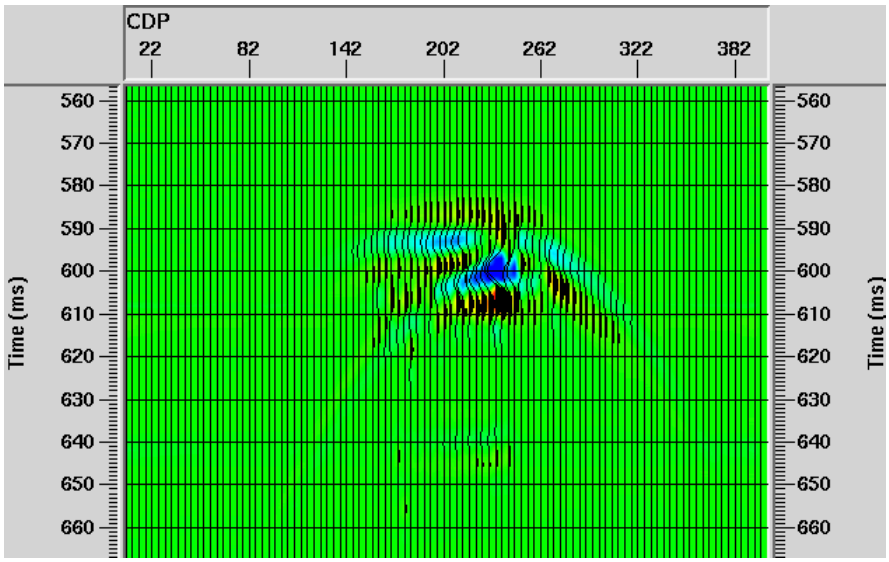

(c) The difference of pre- and post-production seismic responses

Figure 5.12 *PP* stacking seismic sections of pre- and post-production models with wormhole effects using a zero-phase, 60*Hz* Ricker wavelet (Chen, et al. 2004)

Figure 5.13 shows the stacked sections of *PS* seismic data of the pre-production reservoir model and the post-production model, as well as the difference, using the same 60 *Hz* Ricker wavelet. In Figure 5.13b, it is very easy to distinguish the seismic response of the drainage zone with outstanding peaks and troughs, compared with *PP* seismic responses. The reasons could rely on 1) there are higher *S*-wave velocity and density contrasts; 2) *PS* data may have higher resolution due to its relatively short wavelength compared with that of *PP* data for similar frequencies. Another thing easily seen is that the amplitudes increase with the increase in wormhole density (from left to right, correponding to density changes from 2% to 20%). So also do the traveltime delays, increasing can be observed clearly in Figure 5.13c. Therefore, it is possible to use converted waves to better image the distribution of wormholes. Further, converted waves can be employed to detect the most likely orientation of wormhole growth with the variations of amplitude, and provide a valuable, probable drainage pattern to engineers in the field.

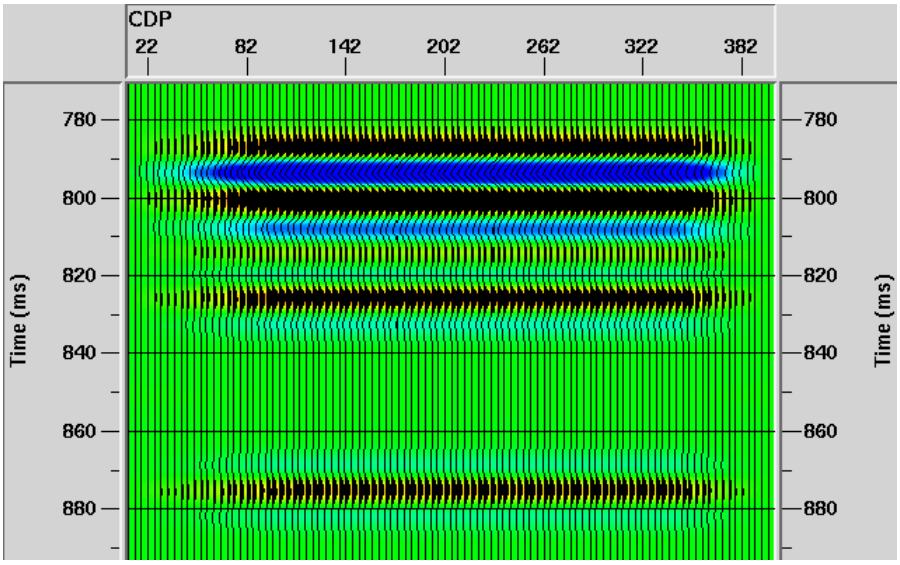

(a) *PS* seismic response of the pre-production model

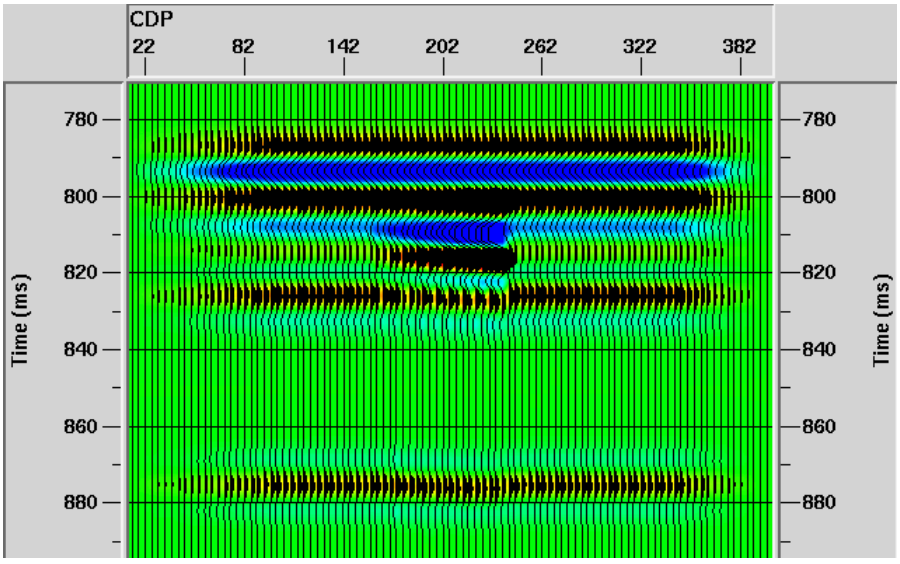

(b) *PS* seismic response of the post-production model in Figure 5.10

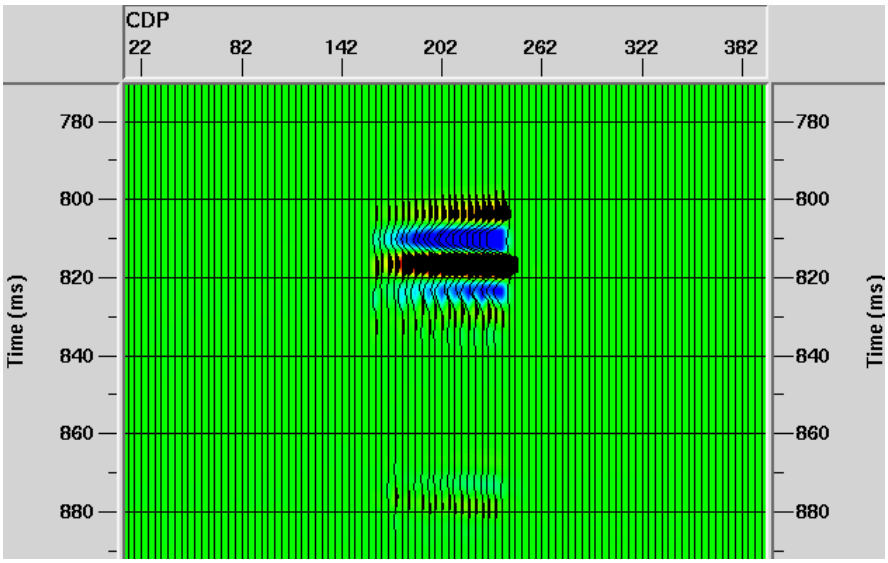

(c) The difference of pre- and post-production seismic responses

Figure 5.13 *PS s*tacking seismic sections of pre- and post-production models with wormhole effects using a zero-phase, 60*Hz* Ricker wavelet (Chen, et al. 2004)

Based on the modelling results, we could conclude that both *PP* and *PS* seismic data can be used imageing the seismic responses of the microscopic effects of wormholes. Because of the greater contrasts in V_s, the amplitude anomalies and travel time delays on the *PS* section are more readily seen than on the *PP* section, where only subtle changes can be detected around CDP 240 where high wormhole densities exist. The increases in amplitudes from CDP 162 to CDP 242 are proportional to the increase of wormhole density, thus possibly predicting the relations between wormhole distributions and amplitude variations.

Althrough both *PP* and *PS* seismic data can be used for imaging the seismic repsonse of the macroscopic effects of wormholes, the thin-bed drainage zones are still challenges to vertical seismic resolution. Figure 5.14 and 5.15 show how seismic frequency restrains the resolution of imaging the amplitude anomalies using 30*Hz* and 90*Hz* Ricker wavelets respectively on both *PP* and *PS* data. In Figure 5.14, using 30*Hz* Ricker wavelet only can hardly see any amplitude anomalies on the *PP* data, while one negative trough anomaly can be observed on *PS* data. However, with 90Hz Ricker wavelet in Figure 5.15, it is clearly seen on *PS* data that there are two peaks above and below the trough anomaly, indicating the exact time of the reflection from the interface at the top of the drainage zone. At the same time, *PP* data also displays a better image of the drainage zone.

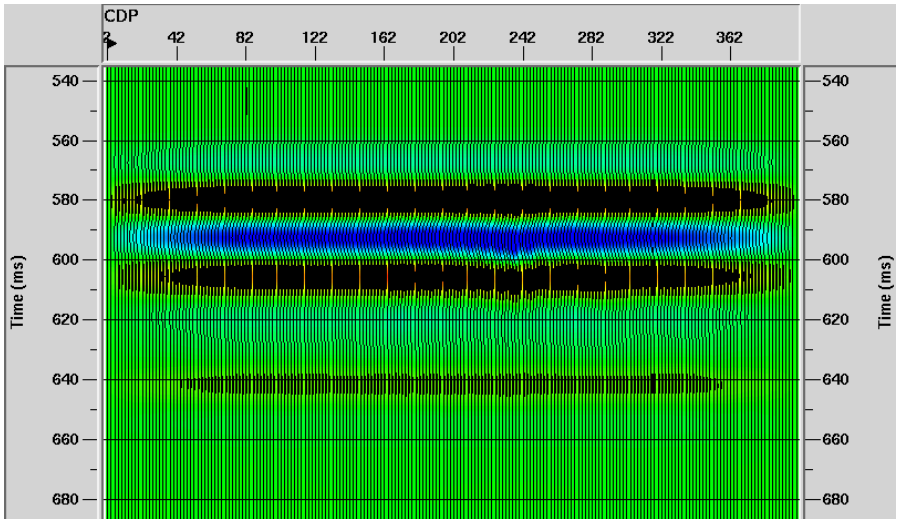

(a) *PP* seismic response

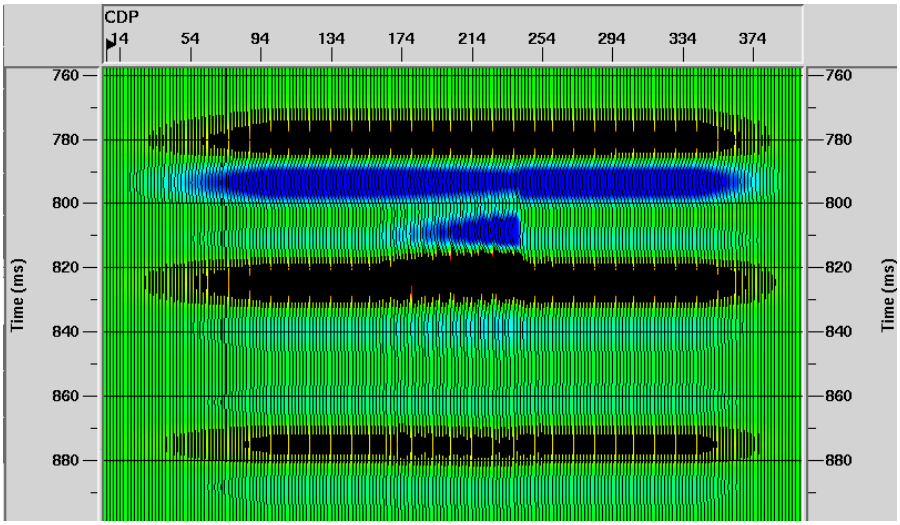

(b) *PS* seismic response

Figure 5.14 Stacking seismic sections of post-production models with wormhole effects using a zero-phase, 30*Hz* Ricker wavelet

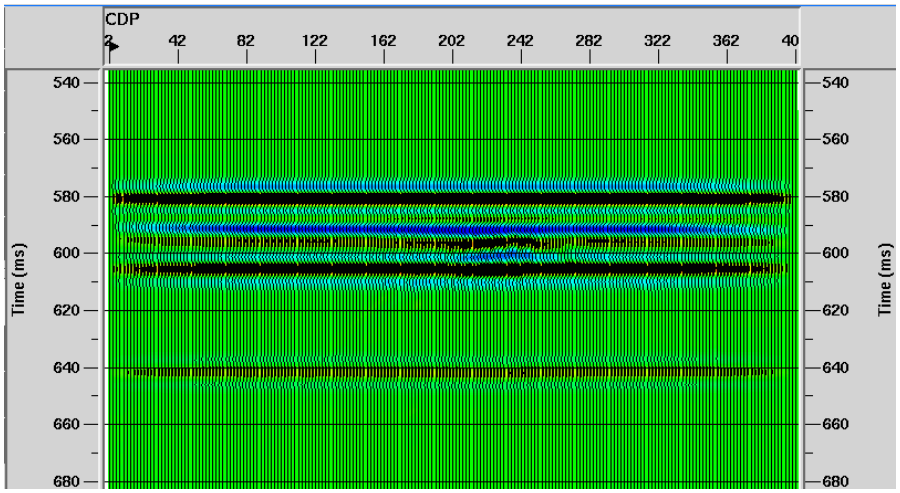

(a) *PP* seismic response

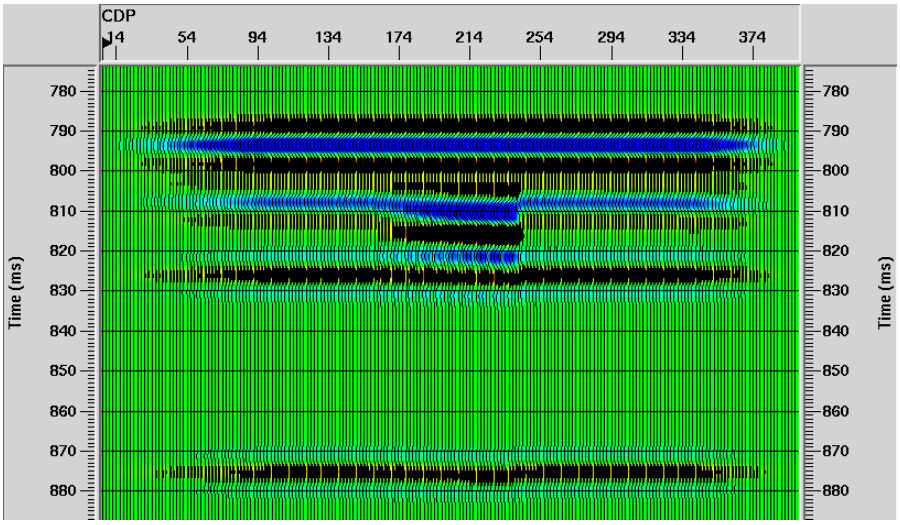

(b) *PS* seismic response

Figure 5.15 Stacking seismic sections of post-production models with wormhole effects using a zero-phase, 90*Hz* Ricker wavelet

5.3 Seismic modeling of both foamy oil and wormhole effects

Above, both foamy oil and wormhole effects on heavy oil cold production have been discussed respectively. In reality, these two cannot be isolated. They both occur during the heavy oil cold production procedure, and the understanding of both are key factors to enhance oil recovery. The amplitude anomalies observed on time-lapse seismic data are also the cumulative responses of these two factors, especially on *PP* seismic data. Therefore, it is necessary to build a combined drainage model to observe the seismic responses of both foamy oil and wormhole effects.

5.3.1 Geological and numerical models

In the field, the drainage zone is defined as the region around the well that has been depressurized, and where oil has been produced. The decrease of the effective reservoir pressure is the key to initiate the formation of foamy oil, which is oil with gas out of solution. Therefore, we think that the foamy oil effects can totally overwhelm the entire drainage zone.

Based on field observations and laboratory simulations, it is believed that the vertical extent of the wormhole zone could be limited within a certain thickness, which can vary from 0.1 to 1, compared with the thickness of the drainage zone. If the thickness

of the drainage zone is relatively thick, the thickness of wormhole layer can be smaller than that. If the thickness of the drainage zone is thin, the thickness of wormhole layer could be equal to that. This is the case in Figure 5.10, where wormhole effects grow through the entire drainage zone.

Here, by considering both foamy oil and wormhole effects, the geological model is illustrated in Figure 2.1, with foamy oil throughout the entire drainage zone, and a wormhole layer developing only within a certain layer of the drainage thickness. And both foamy oil and wormhole effects extend laterally through the whole drainage zone. The schematic of the numerical model is shown in Figure 5.16, where the green coloring represents the foamy oil effects only, and the red coloring is influenced under both foamy oil and wormholes. The thickness of the entire drainage zone is 6m, including a 2m of red coloring zone in the middle. Other layers have the same parameters as the model in Figure 5.10.

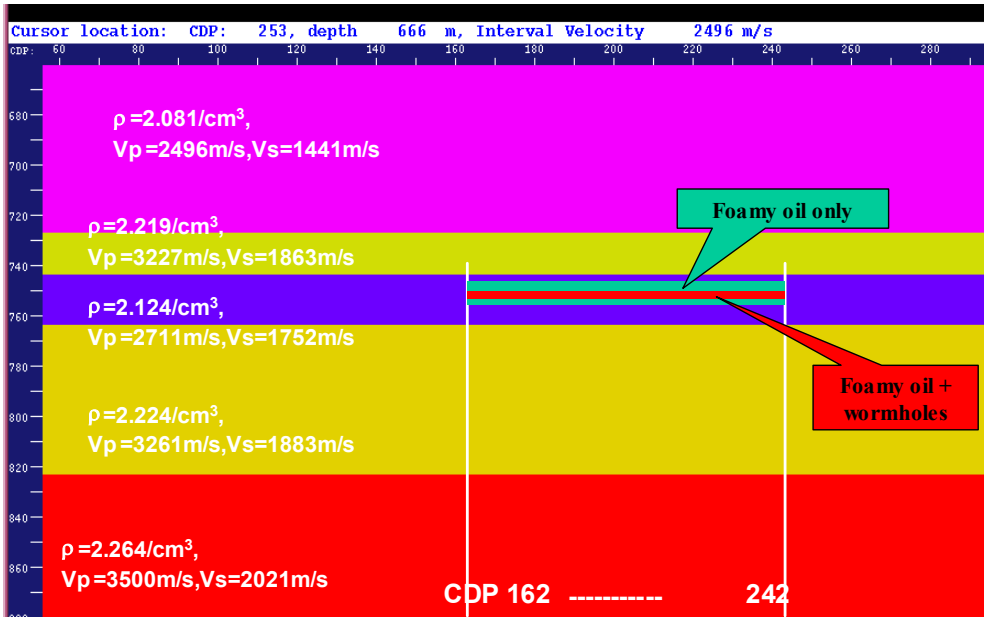

Figure 5.16 Post-production numerical model with both foamy oil and wormhole effects. Within the drainage region with a 6m of thickness, foamy oil zone is in green, the foamy oil and wormhole zone is in red with a thickness of 2*m* (built based on Figure 2.1).

The method used to calculate the mixed fluid bulk modulus of the green zone has been demonstrated in Chapter 4.2. Table 4.2 clearly demonstrates that the existence of free gas could dramatically decrease the mixed fluid bulk modulus by using the uniform mixture status. In our model as we mentioned before, we consider using the average of the uniform and patchy mixtures to represent the fluid mixture. Therefore, the average of mixed fluid bulk modulus of 1.133*Gpa* has been employed to calculate the *P*-wave and *S*-wave velocities, and bulk density of the saturated sands, using Murphy's empirical

relations and the Gassmann's equation, demonstrated in Chapter 4.3. The results are listed in Table 5.2,

Table 5.2 Seismic velocities versus porosity under the average influence of Uniform and Patchy fluid mixture

porosity (100%)	Vp (m/s)	Vs (m/s)	Vp/Vs
0.05	4789.0	3719.9	1.29
0.1	4420.3	3407.4	1.30
0.15	4022.2	3068.5	1.31
0.2	3584.8	2694.1	1.33
0.25	3092.0	2267.5	1.36
0.3	**2512.5**	**1752.3**	**1.43**
0.31	2380.9	1631.7	1.46
0.32	2242.0	1502.1	1.49
0.33	2094.4	1361.0	1.54
0.34	1936.2	1204.5	1.61
0.35	1764.9	1038.7	1.70
0.36	1531.6	762.4	2.01
0.4	1208.2	221.5	5.46
0.41	1186.0	162.6	7.29
0.45	1141.7	47.3	24.15
0.5	**1111.7**	**10.1**	**110.07**
0.55	1090.0	2.2	504.41

Note: the parameters applied to the calculations are derived from the post-production parameters in Table 4.2. The foamy oil zone, defined as a porosity of 30%, have *P* - and *S* - wave velocities of 2512*m/s* and 1752*m/s*, respectively. And the wormhole sands only with a porosity of 50%, have *P*-wave and *S*-wave velocities of 1112*m/s* and 10*m/s*, respectively.

The combined foamy oil and wormhole zone in red in Figure 5.16, is under the influence of both foamy oil and wormholes. Based on the methods described in Chapter 4.3.2, this zone is composed of the foamy oil saturated sand and wormhole sands. The Voigt Upper bound is employed to compute the average *P*-wave and *S*-wave velocities of the combined foamy oil and wormhole zone with wormhole density variations. The results are listed in Table 5.3.

Table 5.3 Seismic velocities versus wormhole density under the average effects of foamy oil and wormholes with the average of the Uniform and Patchy fluid mixtures

wormhole density (100%)	Vs (m/s)	Vp (m/s)	density (kg/cm^3)	Vp/Vs
0	**1752**	**2512**	**2126.6**	**1.43**
0.02	1717.16	2492.66	2119.6	1.45
0.04	1682.32	2473.32	2112.7	1.47
0.06	1647.48	2453.98	2105.7	1.49
0.08	1612.64	2434.64	2098.7	1.51
0.1	**1577.8**	**2415.3**	**2091.7**	**1.53**
0.12	1542.96	2395.96	2084.7	1.55
0.14	1508.12	2376.62	2077.8	1.58
0.16	1473.28	2357.28	2070.8	1.60
0.18	1438.44	2337.94	2063.8	1.63
0.2	**1403.6**	**2318.6**	**2056.8**	**1.65**
0.22	1368.76	2299.26	2049.9	1.68
0.24	1333.92	2279.92	2042.9	1.71

5.3.2 PP and PS seismic data modeling and results

The same GX 2D ray-tracing modeling and Promax processing have been employed to generate the stacked sections of *PP* and *PS* data post-production reservoir

model with both foamy oil and wormhole effects (in Figure 5.16). In this model, there are no wormhole density variations as shown in Figure 5.10. Within the drainage region, the foamy oil zone in green is assigned *P*-wave and *S*-wave velocities of 2512*m/s* and 1752 *m/s*, and density of 2126.6kg/cm^3, and the combining foamy oil and wormhole zone in red has *P*-wave and *S*-wave velocities and densities related to wormhole densities of 20% and 10%, respectively.

Figure 5.17 shows the both *PP* and *PS* stacked sections of the post-production model in Figure 5.16 with a 20% of wormhole density within the combining zone, using a 60*Hz* Ricker wavelet. Figure 5.18 demonstrates the *PP* and *PS* stacked sections of the same model as Figure 5.17, using a 90*Hz* Ricker wavelet. Both figures show amplitude anomalies of the drainage regions associated with both foamy oil and wormhole effects on *PP* data and with wormhole effects on *PS* data. However, it is undetectable for the combined foamy oil and wormhole zone on *PP* data due to its thickness of 2 meters. To image this zone, a much higher seismic frequency is required. Therefore, in reality it is only possible to observe the cumulative footprints of foamy oil and wormholes with typical seismic frequencies.

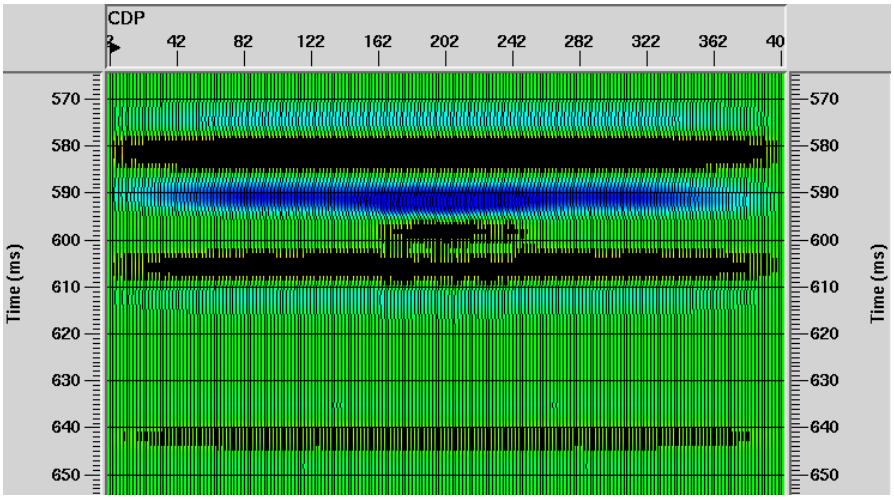

(a) *PP* seismic response

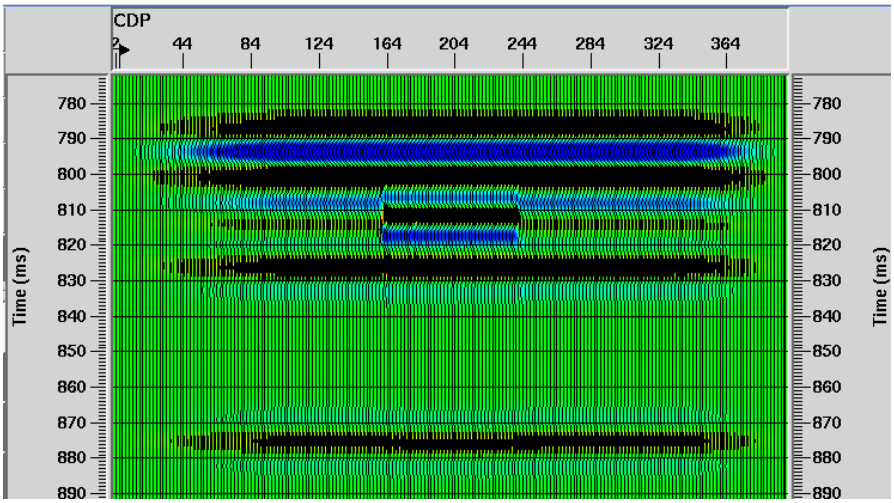

(b) *PS* seismic response

Figure 5.17 Stacked seismic sections of post-production model in Figure 5.16 with a 20% wormhole density using a 60*Hz* Ricker wavelet

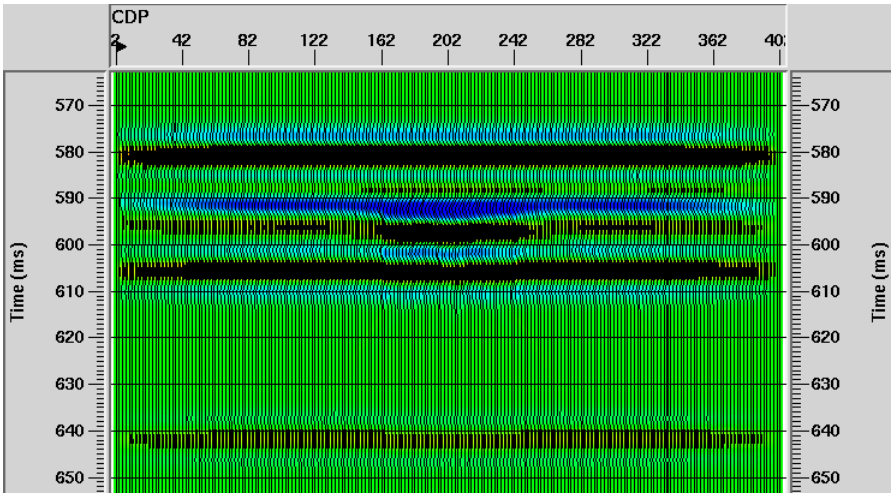

(a) *PP* seismic response

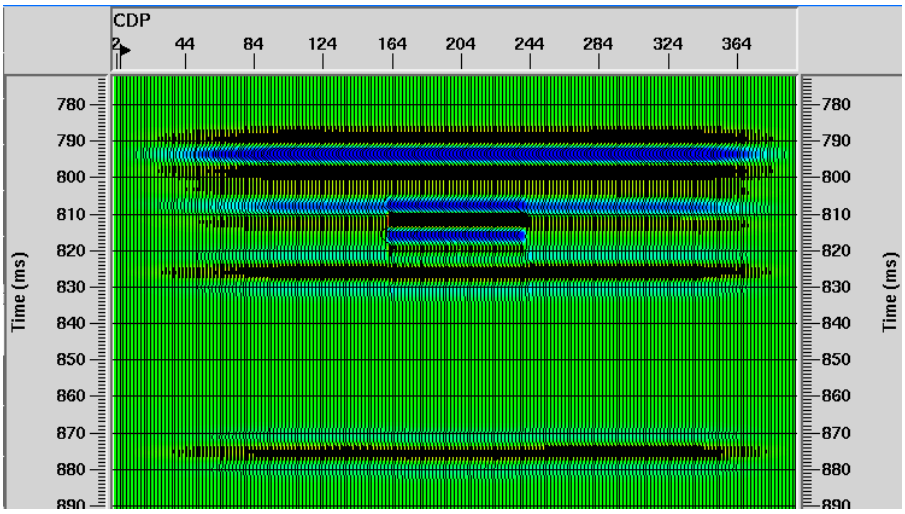

(b) *PS* seismic response

Figure 5.18 Stacked seismic sections of post-production model in Figure 5.16 with a 20% wormhole density using a 90*Hz* Ricker wavelet

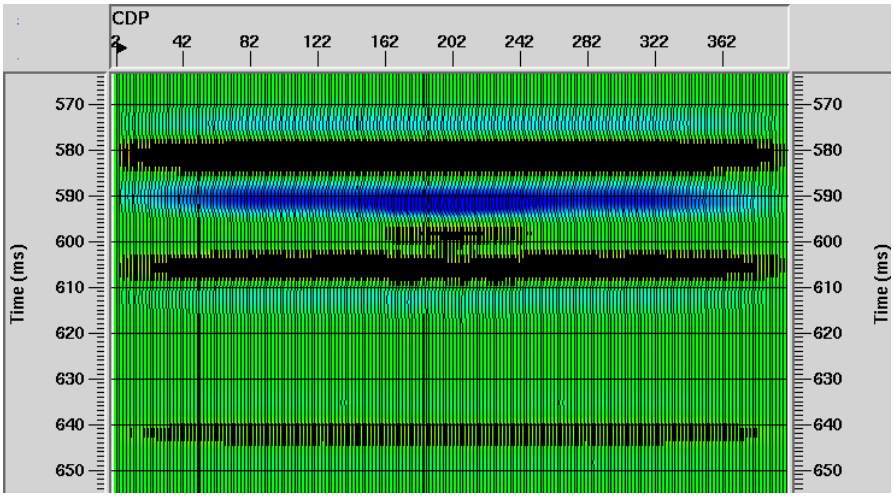

(a) *PP* seismic response

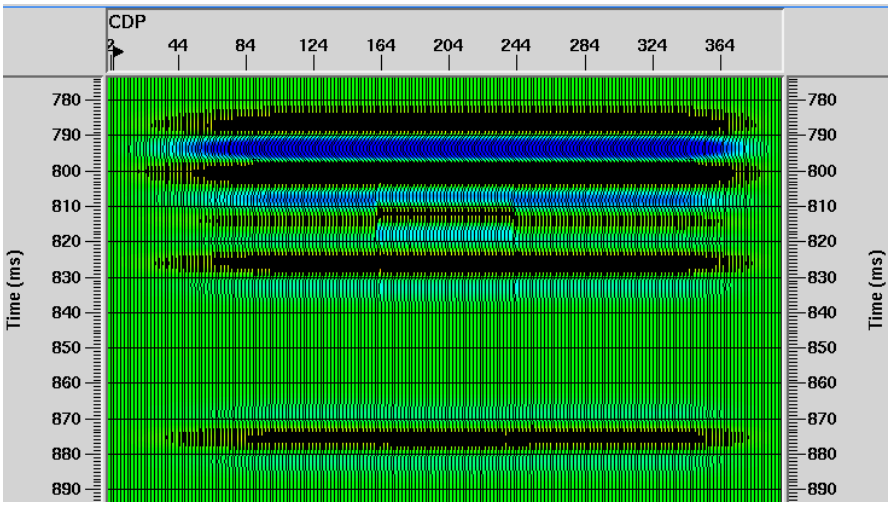

(b) *PS* seismic response

Figure 5.19 Stacked seismic sections of post-production model in Figure 5.16 with a 10% wormhole density using a 60*Hz* Ricker wavelet

Figure 5.19 shows the same *PP* and *PS* stacked sections as Figure 5.17, except with a 10% wormhole density. Comparing these two Figures, we could observe that the higher the wormhole density, the stronger are the cumulative amplitude anomalies.

5.4 Changes of V_p/V_s values within the drainage regions

Based on the above modeling studies, besides the amplitude anomalies and the traveltime delays resulted from the presence of foamy oil and wormholes, it is noticeable that the V_p/V_s within the drainage regions also vary with the changes of the presence of foamy oil and wormholes. Table 5.4 lists the variations of the V_p/V_s in four reservoir situations, including the initial reservoir state, foamy oil effects only, and wormhole effects only, as well as the combined foamy oil and wormhole effects. Figure 5.21 objectively illustrates the relations of V_p/V_s in these four reservoir situations.

Table 5.4 V_p/V_s in four reservoir situations

wormhole density (100%)	wormholes & foamy oil	wormhole only	foamy oil only	initial reservoir
0	1.43	1.55	1.43	1.55
0.02	1.45	1.57	1.43	1.55
0.04	1.47	1.58	1.43	1.55
0.06	1.49	1.60	1.43	1.55
0.08	1.51	1.62	1.43	1.55
0.1	1.53	1.64	1.43	1.55
0.12	1.55	1.67	1.43	1.55
0.14	1.58	1.69	1.43	1.55
0.16	1.60	1.71	1.43	1.55
0.18	1.63	1.74	1.43	1.55
0.2	1.65	1.77	1.43	1.55
0.22	1.68	1.79	1.43	1.55

Note: All V_p/V_s calculated in foamy oil cases consist of 10% gas. In foamy oil only and initial reservoir cases, there are no wormholes developed. Meanwhile, there is a minimized gas effect in the wormhole effects case only.

Figure 5.20 shows that the V_p/V_s in foamy oil case (in red) has the lowest V_p/V_s, because gas only decreases *P*-wave velocity not the *S*-wave velocity. So the existence of gas decreases the V_p/V_s of the drainage region compared with the initial reservoir state (in green). However, in the wormhole only case, we know that the presence of wormholes decreases both *P*-wave and *S*-wave velocities, but causes more decrease in *S*-wave velocity shown in Figure 4.8. Therefore, it has a higher V_p/V_s (in pink) than the initial reservoir V_p/V_s, and continuously increasing with the increase of wormhole density. It is interesting to notice that the V_p/V_s of the drainage region in the foamy oil and wormhole case (in blue) can be either lower and higher than the initial reservoir state with the

variation of wormhole density. In our modeling cases, when the wormhole density is less than 14%, the V_p/V_s of the drainage region has a gas-dominated V_p/V_s, lower than the initial reservoir state. Beyond that, the presence of wormholes dominates the V_p/V_s, resulting in a higher V_p/V_s comparing with the initial V_p/V_s.

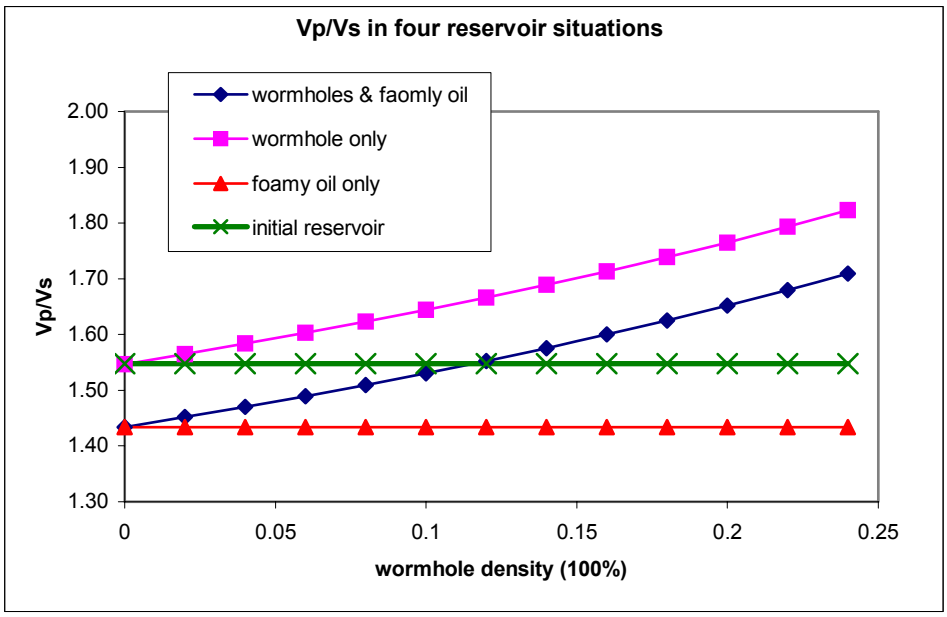

Figure 5.20 The comparisons of V_p/V_s in four reservoir situations (initial reservoir, foamy oil effects only, wormhole effects only, as well as both foamy oil and wormhole effects).

5.5 Chapter summary

Based on the modeling results, it is shown that the heavy oil cold production, by producing sand with oil simultaneously, does cause seismic amplitude anomalies and

traveltime delays on time-lapse seismic data. It provides a useful tool to image the footprints of the reservoir drainage patterns, and can be applied to better design better reservoir development.

In field data, the amplitude anomalies and traveltime delays observed on time-lapse seismic data or post-production survey, are the cumulative responses of both foamy oil and wormhole presences. The modeling results show that both foamy oil and wormholes can cause these anomalies in the *PP* seismic data, but only wormhole effects can result in a significant anomaly in the *PS* seismic data. Therefore, imaging the anomalies in the *PS* data can be employed to detect whether or not there are wormholes developing within the drainage regions. Also, the amplitude anomalies are proportional to the increase of the wormhole density, which can be used to image the distribution of wormhole orientations (Chen, et al., 2004). This is very helpful for engineers in the designing of infill drills in the field.

However, whether using *PP* or *PS* seismic data, there is a limitation to the imaging of these anomalies. That is the seismic resolution. As most of cold production reservoirs are thin, high frequencies are required to achieve discernible resolution.

CHAPTER 6: Conclusions and recommendations

Simultaneous extraction of oil and sand during the cold production of heavy oil generates high porosity channels termed “wormholes”. These highly permeable wormhole channels have been observed in post-production logging and radioactive tracer tests in the field. The development of wormholes causes reservoir pressure to fall below the bubble point, resulting in dissolved-gas coming out of solution to form foamy oil. Both foamy oil and wormholes are believed to be two key factors in the enhancement of oil recovery.

Amplitude anomalies in the vicinity of the borehole observed in time-lapse seismic surveys are possibly a result of the presence of foamy oil and wormholes. These results can be used to image the drainage pattern for infill drilling designs. The use of time-lapse reflection seismology for detecting the presence of foamy oil and wormholes is discussed in this thesis. Our study includes three major factors that influence time-lapse reflection seismology: foamy oil effects only, wormhole effects only, and the joint effects of these two factors.

Our results lead to the following conclusions:

1. The presence of small amounts of gas trapped in the foamy oil can dramatically decrease the fluid bulk modulus, reducing the *P*-wave velocity of saturated sands, thus resulting in the negative amplitude anomalies within the drainage regions when considering the fluid as a uniform fluid mixture (Reuss model). Elastic moduli and velocities under gas influence, obtained by using the average of Reuss and Voigt bounds, have been applied to an in-situ reservoir in a Western Canadian heavy oil field. 2D numerical seismic responses of foamy oil within drainage areas show amplitude anomalies and traveltime delays when pre- and post-production results are compared.

2. By ignoring the effects of foamy oil, wormholes with porosities greater than the critical porosity can strongly change the rigidity and frame bulk modulus of the reservoir sands, thus resulting in the decrease of both *P*- and *S*-wave velocities of the wormhole sands based on Murphy's empirical relations.

3. However, only the macroscopic effects of wormholes on *P*- and *S*-wave velocities of the reservoir rock can be observed, when large amount of sands are produced. Individual wormholes cannot be imaged because their diameters are of the order of

centimeters, much lower than the resolving ability of typical seismic frequencies. The Voigt upper bound is applied to the computation of the cumulative effects of wormholes on the saturated sands. The changes in both *P*-wave and *S*-wave velocities appear to be proportional to wormhole density.

4. 2D numerical models designed to examine cumulative effects of wormholes using both *PP* and *PS* seismic data indicate that *PS* data are better at imaging the wormhole footprints. This is due to the *S*-wave velocity being more sensitive to the presence of wormholes. Again, the increases in amplitude anomalies and traveltime delays are proportional to wormhole density.

5. The seismic responses of joint foamy oil and wormhole models show the amplitude anomalies and traveltime delays on both *PP* and *PS* data, with better images of wormholes being produced in *PS* seismic data. However, the thin wormhole layer within the drainage region cannot be detected due to its thickness. Therefore, the anomalies observed in *PP* data demonstrate the cumulative responses of both foamy oil and wormholes, while those on *PS* data only represent the wormhole impact. By considering the cost, we think that there is no need shot pre-production muitl-

component survey, and the post-production multi-component survey could be enough to image the effects of wormholes based on modeling results.

6. Considering that most of cold production reservoirs are thin, high frequencies are required to achieve discernible resolution.

7. Comparing with the initial reservoir state, the V_p/V_s of the post-production reservoir with both foamy oil and wormhole effects can be higher or lower, depending on whether it is foamy oil dominant or wormhole dominant. Because the presence of gas decreases *P*-wave velocity and does nothing with *S*-wave velocity, this leads to a low V_p/V_s for the foamy oil situation. While the presence of wormholes decreases both *P*- and *S*-wave velocities, and more on *S*-wave velocity, leading to a higher V_p/V_s compared to the V_p/V_s of the initial reservoir.

Based on the results of this study, I recommend the following future research:

1. Field 3D time-lapse multicomponent seismic data should be applied to the analysis of both foamy oil and wormhole effects. Both *PP* and *PS* data could be employed to examine the validity of the methodology used in this thesis study;

2. Post-production logging can be an implement tool to provide significant data for model designs and verification of the modeling results;
3. AVO (Amplitude versus Offset) analysis can be an interesting means for detecting foamy oil and wormhole effects in heavy oil cold production;
4. High resolution and cross-borehole seismic surveys can be used to better image the distribution of wormholes;
5. Extend Gassmann's equation to high viscosity fluid;
6. Borehole gravity changes, resulting from producing sands, can be an alternative to image the wormhole distribution.

REFERENCES

Bachrach, R., Dvorkin, J. and Nur, A.M., 2000, 'Seismic velocities and Poisson's ratio of shallow unconsolidated sands', Geophysics, 65, 559-564.

Batzle, M. and Wang, Z., 1992, 'Seismic properties of pore fluid', Geophysics, 57, 1396-1408.

Benson, A.K. and Wu, J., 1999, 'A modeling solution for prediction (a) dry bulk modulus, rigidity modulis and (b) seismic velocities and reflection coefficients in porous, fluid-filled rocks with applications to laboratory rock samples and well logs', Journal of Applied Geophysics, 41, 49-73.

Bentley, R.L., Zhang, J. and Lu, H., 1999, 'Four-D seismic monitoring feasibility', CREWES Research Report, Volume 11.

Castagna, J.P. and Backus, M.M., 1993, 'Offset Dependent Reflectivity – Theory and Practice of AVO Analysis', SEG publication, Tulsa.

Chacho, A., 1989, 'Porosity indentification using amplitude variations with offset: Examples from South Sumatra', Geophysics, 54, 942-951.

Chen, S., Lines, L. and Daley, P., 2004, 'Foamy oil and wormhole footprints in heavy oil cold production reservoirs', Recorder, Canadian Society of Exploration Geophysicists, October, volume 29.

Chung, H. and Lawton, D., 1995, 'Amplitude responses of thin beds: Sinusoidal approximation versus Ricker approximation', Geophysics, 60, 223-230.

Domenico, S.N., 1976, 'Effect of brine-gas mixture on velocity in an unconsolidated sand reservoir', Geophysics, 41, 882-894.

Downton, J., 2001, 'A rock physics framework for interpreting reservoir properties from seismically-derived elastic parameters', Scott Pickford.

Dunn, L.J., Mathews, C.M. and Zahacy, T.A., 1995, 'Progressing cavity pumping system application in heavy oil production', SPE 30271.

Dusseault, M., 1994, 'Mechanisms and management of sand production', C-FER project 88-06, volume 4.

Gassmann, F., 1951, 'Uber die elastizitat poroser medien: Verteljahrsschrift der Naturforschenden Gesellschaft in Zurich,96, 1-23.

Gist, G.A., 1994, ' Interpreting laboratory velocity measurements in partially gas-saturated rocks', Geophysics, 59, 1100-1109.

Gregory, A.R., 1976, 'Fluid saturation effects on dynamic elastic properties of sedimentary rocks', Geophysics, 41, 895-921.

Hornby, B.E. and Murphy, W.F., 1987, 'Vp/Vs in unconsolidated oil sands: Shear from Stoneley', Geophysics, 52, 502-513.

Lines, L.R., Chen, S., Daley, P.F., and Embleton, J., 2003, ' Seismic pursuit of wormholes', The Leading Edge, May.

Maini, B.B., 2004, 'Foamy oil flow in cold production of heavy oil', Distinguished lecture, Petroleum Society of C.I.M., April.

Mavko, G. and Mukerji, T., 1998, 'Bounds on low-freauency seismic velocities in partially saturated rocks', Geophysics, 63, 918-924.

Mavko, G. and Mukerji, T., 1998b, 'Comparison of the Kiref and critical porosity models for prediction of porosity and Vp/Vs', Geophysics, 63, 925-927.

Mayo, L., 1996, ' Seismic monitoring of foamy heavy oil, Lloydminster, Western Canada', SEG Expanded Abstracts.

Metwally, M. and Solanki, S.C., 1995, 'Heavy oil reservoir mechanisms, Linbergh and Frog Lake Fields, Alberta, Part 1: Field observations and reservoir simulation', 46th annual technical meeting of the Petroleum Society of CIM, Banff, Alberta.

Miller, 2001, ' Air injection recovery of cold-produced heavy oil reservoirs', presented at CIPC Conference of the Petroleum Society in Calgary.

Murphy.W, Reischer, A. and Hsu, K., 1993, 'Modulus decomposition of compressional and shear velocities in sand bodies', Geophysics, 58, 227-239.

Mayo, L., 1996, 'Seismic monitoring of foamy heavy oil, Lloydminster, Western Canada', 66th Ann. Internat. Mtg. Soc. Of Expl. Geophys, 2091-2094.

Nur, A., Mavko, G., Dvorkin,J. and Galmudi, D., 1998, 'Critical porosity: A key to relating physical properties to porosity in rocks', The Leading Edge, 357-362.
Prasad, M., 2002, ' Acoustic measurements in unconsolidated sands at low effective pressure and overpressure detection', Geophysics, 2002, 67, 405-412.

Sawatzky, R.P., Lillico, D.A., London, M.J., Tremblay, B.R., and Coates, R.M., 2002, ' Tracking cold production footprints', CIPC conference, Calgary, Alberts.

Spencer, J.W, Michael, Jr., Cates, E. and Thompson, D.D, 1994, 'Frame moduli of inconsolidated sands and sandstones', Geophysics, 59, 1352-1361.

Squires, A., 1993, 'Inter-well Tracer Results and Gel Blocking Program', paper presented at the 10th annual meeting of the Canadian Heavy Oil Association, Calgary, March.

Tichelaar, A.W. and Klaas W., 1995, 'Sonic logging of compressional-wave velocities in a very slow formation', Geophysics, 60, 1627-1638.

Tremblay, B., Sedgwick, G. and Vu, D., 1999a, 'A review of cold production in heavy oil reservoirs', EAGE-10th European Symposium on Improved Oil Recovery, Brighton, UK.

Tremblay, B., Sedgwick, G. and Vu, D., 1999b, ' CT Imaging of Wormhole Growth under Solution-Gas Drive', SPE Reservoir Eval. & Eng., February.

Tremblay, B. and Oldakowski, K., 2002, 'Wormholes growth and interaction in a large sand pack', Journal of Petroleum Science and Engineering, 34, 13-34.

Wang, Z., 2001, 'Fundamental of seismic rock physics', Geophysics, 66, 398-412.

Wang, Z., Batzle, M. and Nur, A.M., 1990, 'Effect of different pore fluids on seismic velocities in rocks', Canadian Journal of Exploration Geophysics, 26, 104-112.

Widess, M.B., 1973, ' How thin is a thin bed?', Geophysics, 38, 1176-1180.

Wyllie, M. R. J., Gregory, A. R., and Gardner, L. W., 1956, ‘Elastic wave velocities in heterogeneous and porous media’, Geophysics, 21, 41-70.

Woods, A. B., 1941, ‘A textbook of sound: G.Bell and Sons’.

Yuan, J., Tremblay, B., and Babchin, A., 1999, ‘A wormhole network model of cold productin in heavy oil’, SPE 54097.

Zou, Y and Bentley, L., 2001, ‘ “FluidSeis” user’s guide (a Matlab fluid substation program)’, CREWES Research Report, 13.